© 2017. Published by The Company of Biologists Ltd | Journal of Cell Science (2017) 130, 177-189 doi:10.1242/jcs.190967

SPECIAL ISSUE: 3D CELL BIOLOGY

RESEARCH ARTICLE

Deep nuclear invaginations are linked to cytoskeletal filaments – integrated bioimaging of epithelial cells in 3D culture

Danielle M. Jorgens[1,2,*], Jamie L. Inman[3,*], Michal Wojcik[4,*], Claire Robertson[3,*], Hildur Palsdottir[1], Wen-Ting Tsai[1], Haina Huang[4], Alexandre Bruni-Cardoso[3,5], Claudia S. López[2], Mina J. Bissell[3,‡], Ke Xu[1,4] and Manfred Auer[1,‡]

ABSTRACT

The importance of context in regulation of gene expression is now an accepted principle; yet the mechanism by which the microenvironment communicates with the nucleus and chromatin in healthy tissues is poorly understood. A functional role for nuclear and cytoskeletal architecture is suggested by the phenotypic differences observed between epithelial and mesenchymal cells. Capitalizing on recent advances in cryogenic techniques, volume electron microscopy and super-resolution light microscopy, we studied human mammary epithelial cells in three-dimensional (3D) cultures forming growth-arrested acini. Intriguingly, we found deep nuclear invaginations and tunnels traversing the nucleus, encasing cytoskeletal actin and/or intermediate filaments, which connect to the outer nuclear envelope. The cytoskeleton is also connected both to other cells through desmosome adhesion complexes and to the extracellular matrix through hemidesmosomes. This finding supports a physical and/or mechanical link from the desmosomes and hemidesmosomes to the nucleus, which had previously been hypothesized but now is visualized for the first time. These unique structures, including the nuclear invaginations and the cytoskeletal connectivity to the cell nucleus, are consistent with a dynamic reciprocity between the nucleus and the outside of epithelial cells and tissues.

KEY WORDS: Integrated bioimaging, Cytoskeleton, Mechanotransduction, Human mammary epithelial cells, Nucleoplasmic reticulum, Extracellular matrix

INTRODUCTION

The three-dimensional (3D) architecture adopted by cells in response to microenvironmental stimuli plays a crucial role in their function within tissues. When cells are removed from their native organs and placed in two-dimensional (2D) cultures, they essentially lose all tissue-specific functions. Malignant cells can be induced to form phenotypically normal-like structures in 3D culture. These structures are phenotypically reverted and behave like those of non-malignant cells; they fail to form tumors (Bissell and Hines, 2011; Bussard and Smith, 2012; Weaver et al., 1997) and normalize their pattern of gene expression (Becker-Weimann et al., 2013). Our findings and those from other laboratories show clearly that the 3D architecture of the tissues, and the cells within them, regulate and are regulated by their biological state. We submit that cell and tissue polarity, regulated through the cytoskeleton, allows for a signaling connection from the extracellular matrix (ECM), through the organization of the plasma membrane, to the nuclear envelope and the nucleoplasm.

Recent work has shown clearly that many previously unexplored aspects of 3D architecture, such as the organization of the nuclear envelope, are not stochastic or cell intrinsic – the structure and composition of the nuclear envelope responds to microenvironmental stimuli with important consequences for gene regulation (Bissell and Labarge, 2005; Boudreau et al., 1995b; Hagios et al., 1998; Kim and Wirtz, 2015; Spencer et al., 2011; Versaevel et al., 2014; Xu et al., 2009, 2010). Even before the advent of 3D cultures, Bissell and colleagues proposed that ECM must signal through receptors, via the cytoskeleton, through nuclear matrix to chromatin to control tissue-specific function and vice versa (Bissell et al., 1982), with the concept being further extended by Boudreau et al. in 1995 (Boudreau et al., 1995a). This possibility has found much support through the literature both from the Bissell laboratory as well as others that there is physical linkage between the ECM through ECM receptors and the cytoskeleton, which in turn connects to the nuclear envelope receptors to physically couple to chromatin (Tapley and Starr, 2013). Even in traditional cell culture on flat substrata (2D cell culture), intriguing studies performed nearly 20 years ago made clear that the nucleus is mechanically linked to the plasma membrane through the cytoskeleton, and further, that under mechanical strain the nuclear morphology can be greatly altered (Bhat and Bissell, 2014; Hu et al., 2005; Maniotis et al., 1997; Osorio and Gomes, 2014; Zhu et al., 2014). These and a number of other studies raise the question 'what are the essential 3D architectural elements in the interconnected network of the nucleus, cytoskeleton and ECM in cells forming quiescent organotypic 3D structures that are akin to those *in vivo*?'.

Mammary-gland-specific functions of epithelia, such as quiescence, basal–apical polarity or, in murine cells, production of milk proteins, can be recapitulated in biomimetic cultures in 3D. In laminin-rich gels, single non-malignant mammary epithelial cells undergo 'cohesive angular motion', immediately adopt apical–basolateral polarity, divide with unequal stem-like divisions while adhering to each other and all the while physically rotating until, between 7 and 10 days, they become quiescent (Tanner et al., 2012). Non-malignant epithelial cells in biomimetic cultures develop this polarized 3D architecture over time and resemble mammary acini, whereas cells that are cultured on traditional flat polystyrene show

[1]Molecular Biophysics and Integrated Bioimaging Division, Lawrence Berkeley National Laboratory, 1 Cyclotron Road, MS Donner, Berkeley, CA 94720, USA. [2]Department of Biomedical Engineering, Oregon Health and Science University, 3181 Sam Jackson Park Road, Portland, OR 97239, USA. [3]Biological Systems and Engineering Division, Lawrence Berkeley National Laboratory, Berkeley, CA 94720, USA. [4]Department of Chemistry, University of California, Berkeley, CA 94720, USA. [5]Department of Biochemistry Instituto de Quimica, Universidade de Sao Paulo, Sao Paulo, 05508-000, Brazil.
*These authors contributed equally to this work

[‡]Authors for correspondence (MJBissell@lbl.gov; MAuer@lbl.gov)

D.M.J., 0000-0002-7143-0118; H.P., 0000-0002-2664-9305; M.A., 0000-0002-5435-9436

Received 13 April 2016; Accepted 28 July 2016

Journal of Cell Science (2017) 130, 177-189 doi:10.1242/jcs.190967

only limited polarity in monolayers when reaching confluence. Although it is clear that the cellular architecture is regulated by the microenvironment, how the ECM connects to the nucleus remains incompletely understood. This is because there are serious resolution limits to traditional optical microscopy, as well as the challenges of using sub-100-nm resolution techniques in crowded 3D embedded cultures.

To address the issues of architecture at the level of the whole cell, we analyzed the 3D architecture of non-malignant human breast epithelial cells in acinar-like structures using a number of complementary imaging approaches, including high-resolution 2D transmission electron microscopy (TEM), electron tomographic volume microscopy, focused ion beam scanning electron microscopy (FIB-SEM), as well as confocal and super-resolution immunofluorescence imaging, including stochastic optical reconstruction microscopy (STORM). We found that non-malignant cells in 3D culture showed deep invaginations into and tunnels through the nucleus; these invaginations house cytoskeletal filaments that then connect to the nuclear envelope. These findings establish for the first time the structure of the physical connection between the nucleus and cell adhesion sites, providing a promising mechanical link between the cell's microenvironment and the nucleus.

RESULTS

HMT-3522-S1 cells in biomimetic 3D tissue culture show growth arrest and an unexpected organization

In order to study the nuclear and cytoskeletal architecture of mammary epithelial cells with high-resolution, we chose to use a well-characterized non-malignant human mammary epithelial cell (HMEC) line, HMT-3522-S1 (S1) (Briand et al., 1987; Petersen et al., 1992). We grew the S1 cells in a laminin-rich ECM (lrECM) 3D tissue culture over the course of 10 days with EGF withdrawal at day 7, when the acini were formed. We found that nearly all of the cells in acini at day 10 were growth-arrested (Fig. 1A). Only two in 5317 cells examined had incorporated EdU during a 24-h labeling period, and thus were determined to be proliferating (0.0003%). In contrast, in tumorigenic HMT-3522-T4 cells, stained as a positive control, 97% of cells had incorporated the EdU label during the 24-h period (Fig. 1A, insert). S1 acini varied in size, and the number of nuclei per acinus ranged from 5 to 20, with most of the acini showing 9–12 nuclei per acinus (Fig. 1B). Consistent with our previous work, we observed immunofluorescent staining for the Golgi (GM130) that was positioned towards the acinar center as well as apical localization of the tight junction protein zona occludens-1 (ZO-1) in 57.7% of the acini (Fig. 1C–E). β-catenin was positioned basolaterally (Fig. 1F), and the hemidesmosome-associated protein α6 integrin as well as actual hemidesmosomes (Fig. 1G,H) localized to the acinar periphery (i.e. basal surface of the cells of the acinus), indicating appropriate apical–basal polarity, consistent with previous work (Plachot et al., 2009; Weaver et al., 2002, 1997). Furthermore, we found the ultrastructural phenotype described to be very consistent, even when acini were grown on top of the 3D culture instead of being fully immersed in the 3D lrECM (Lee et al., 2007).

We examined embedded acini as whole-mounts by using light microscopy and noted a range of different sizes, typically ranging ∼20–50 µm (Fig. 1I). Semi-thin sections of 500 nm were imaged with optical light microscopy upon Toluidine-Blue staining (Fig. 1J). We found that the size of each cell (in a cross-section) in each acinus was fairly similar, and that size differences of acini were explained by differences in the number of cells per acinus (Fig. 1J–L), which is consistent with our results on the nuclei number per acinus shown in Fig. 1B. With transmission electron microscopy, we imaged acini of different sizes (Fig. 1K–M) and discovered the cells were not as closely associated as expected from the immunofluorescence data. In order to evaluate a larger volume of a typical acinus than is possible by performing traditional TEM, we turned to a serial sectioning approach, followed by serial TEM imaging of 22 thin resin sections, each with a nominal thickness of 100 nm. Serial section TEM (Fig. 1M–M‴) across a total depth of ∼2 µm revealed the cells had intermittent junction points along their lateral surfaces and, although there was apical polarity as measured by determining the immunofluorescence of ZO-1 in the apical space, no true lumen with tight junctions were observed (Movie 1). Interestingly, whereas optical light microscopy analysis of Toluidine-Blue-stained semi-thin sections and electron micrographs clearly show the intercellular spaces, confocal immunofluorescence microscopy of β-catenin showed continuous staining, revealing that the resolution limit of light in fluorescence microscopy can lead to a false interpretation of lateral membrane organization (Fig. 1F,J,K,L).

Desmosomes flanked by membrane protrusions comprised basolateral organization in acini that had been optimally preserved

To examine the cell–cell interactions in more detail, we performed high-resolution TEM imaging (Fig. 2). The cellular ultrastructure showed exquisite preservation owing to the ultra-rapid freezing and the freeze-substitution process (McDonald and Auer, 2006; Triffo et al., 2008), otherwise known as high-pressure freezing with freeze substitution (HPF-FS). The compact spacing of elements within the cytoplasm (Fig. 2A) displayed exquisite preservation, as indicated by dense cytoplasm, free of signs of extraction or aggregation, which contained cytoskeleton radiating from cell–cell adhesion sites (Fig. 2B,C). The sites of cell–cell adhesion occurred in a spot-like pattern flanked on either side by microvilli-like structures (Fig. 2A–C). The adhesion complexes typically bridged a ∼30–35-nm-wide gap, with prominent and well-defined ∼10–15-nm-thick dark bands on the cytoplasmic side of the plasma membrane (Fig. 2D,E).

To gain insight into the 3D macromolecular architecture of such adhesion sites, we employed electron tomography (Fig. 2F), in which ∼1-nm-thin slices through the 3D tomogram revealed straight filaments that crossed the gaps perpendicular to the flanking plasma membranes. Given the dimensions of the filaments, bridging a 30–35-nm-wide gap, as well as the uniform cytoplasmic thickness and the cytoskeletal connectivity, we identified these junctions to be predominantly macula adherens (desmosomes) (Movie 2) (Al-Amoudi et al., 2007). The junctions identified in Fig. 2 are unlikely to be another type of common cell–cell junctional complex present in epithelial cells, zonula adherens junctions. We did observe occasional small adherens junctions that spanned ∼15–25 nm between adjacent cell membranes, but through ultrastructural analysis did not correspond to the expected numbers of zonula adherens junctions that had been indicated by the staining of β-catenin (Fig. 1F). It is worth noting that despite the apical ZO-1 staining (Fig. 1C), we rarely observed zonula occludens (tight junctions).

In the areas between the desmosomal adhesion sites, the cells were typically much further apart (several hundred nanometers; Fig. 2A–C). In these, spaces we found plasma-membrane-bound protrusions that, when cut longitudinally or in cross-section, resembled microvilli. The fact that desmosomes, which represent

Journal of Cell Science (2017) 130, 177-189 doi:10.1242/jcs.190967

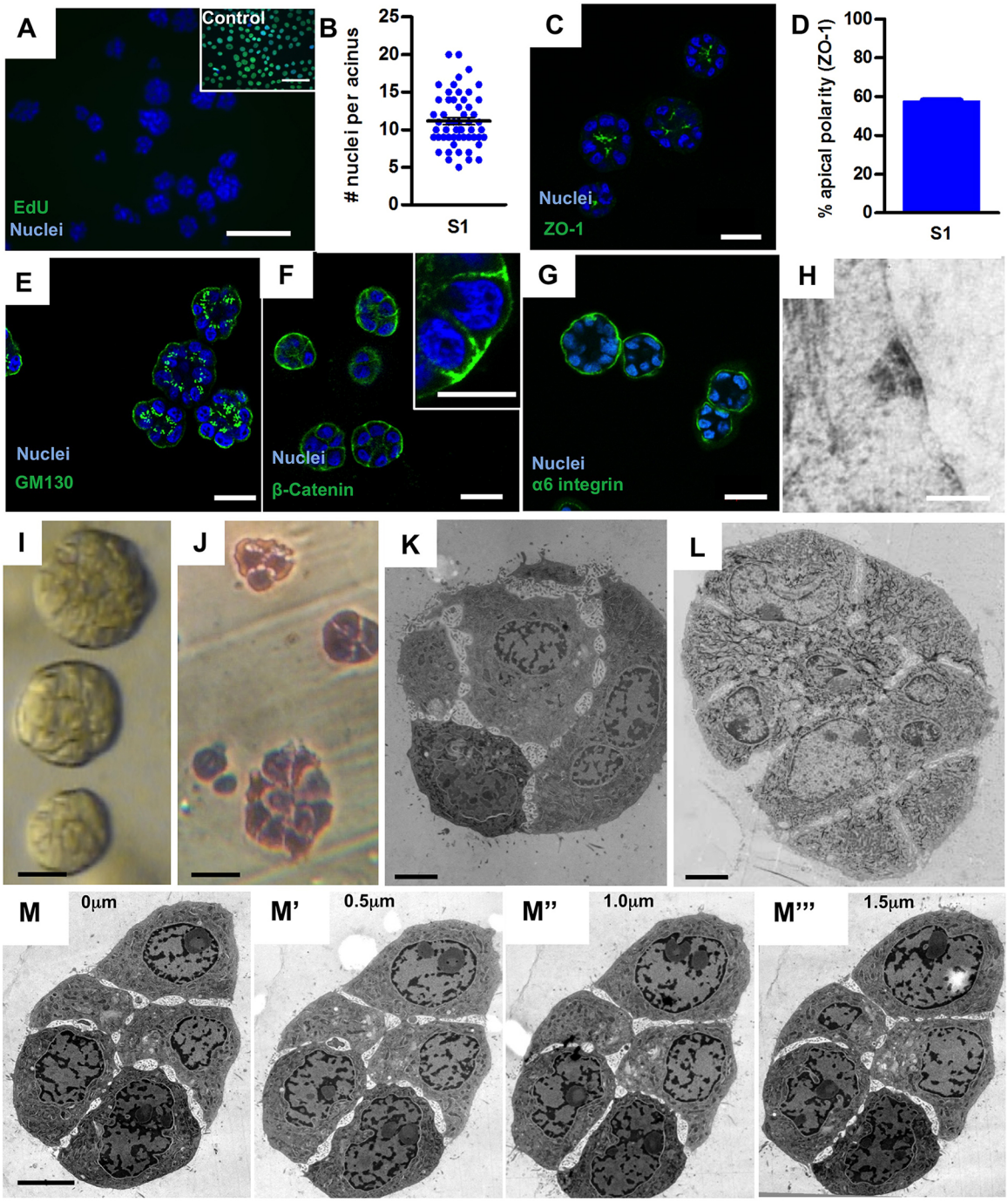

Fig. 1. Growth-arrested S1 acini show little evidence of lumen, and unexpected cell–cell interactions in 2D electron micrographs and serial section TEM. (A) At 10 days of growth in lrECM, S1 acini demonstrate growth arrest with 98.8% of cells not incorporating EdU (*n*=5317 cells in three independent experiments). Inset, control T4-2 cell incorporation of EdU at 24 h (*n*=2006 cells in two replicates). (B) Using DAPI staining, the average number of nuclei per acinus was determined to be 11.16 (*n*=55 acini counted in two independent experiments). Acini displayed apical polarity based on (C) ZO-1 staining oriented at the apical surface (D); when quantified, 57.7% of the acini displayed apical polarity (*n*=592 acini counted in two independent experiments). Representative immunofluorescence staining for apico–basal polarity in acini with antibodies recognizing the (E) Golgi (GM130), (F) β-catenin (inset, higher magnification) and (G) α6 integrin. (H) TEM analysis of the basal surface of acini revealed hemidesmosomes. Light micrographs of S1 acini prepared for TEM analysis: (I) polymerized in epon–araldite resin and (J) 500-nm semi-thin cross-section through acini. TEM analysis of acini (K–M) revealed electron-lucid intercellular spaces, which (M–M‴) serial sectioning demonstrated are continuously present along the cell surfaces, as viewed every 0.5 µm. Scale bars: 100 µm (A); 20 µm (C,E,F,G); 10 µm (inset of F); 200 nm (H); 25 µm (I); 25 µm (J); 5 µm (K–L); 5 µm (M–M‴).

a basolateral marker, and microvilli, which represent an apical marker, are in close proximity without separation by a tight junction (Fig. 2B,C) suggests that acinar cells no longer display *in vitro* the strict apical–basolateral polarity that is a hallmark of fully differentiated epithelial tissues *in vivo*. Instead, cells showed reduced polarity with cellular surfaces that faced the ECM still forming hemidesmosomes (Fig. 1H); yet, they lacked continuous and apically located tight junctions and, thus, did not have a sealed

Journal of Cell Science (2017) 130, 177-189 doi:10.1242/jcs.190967

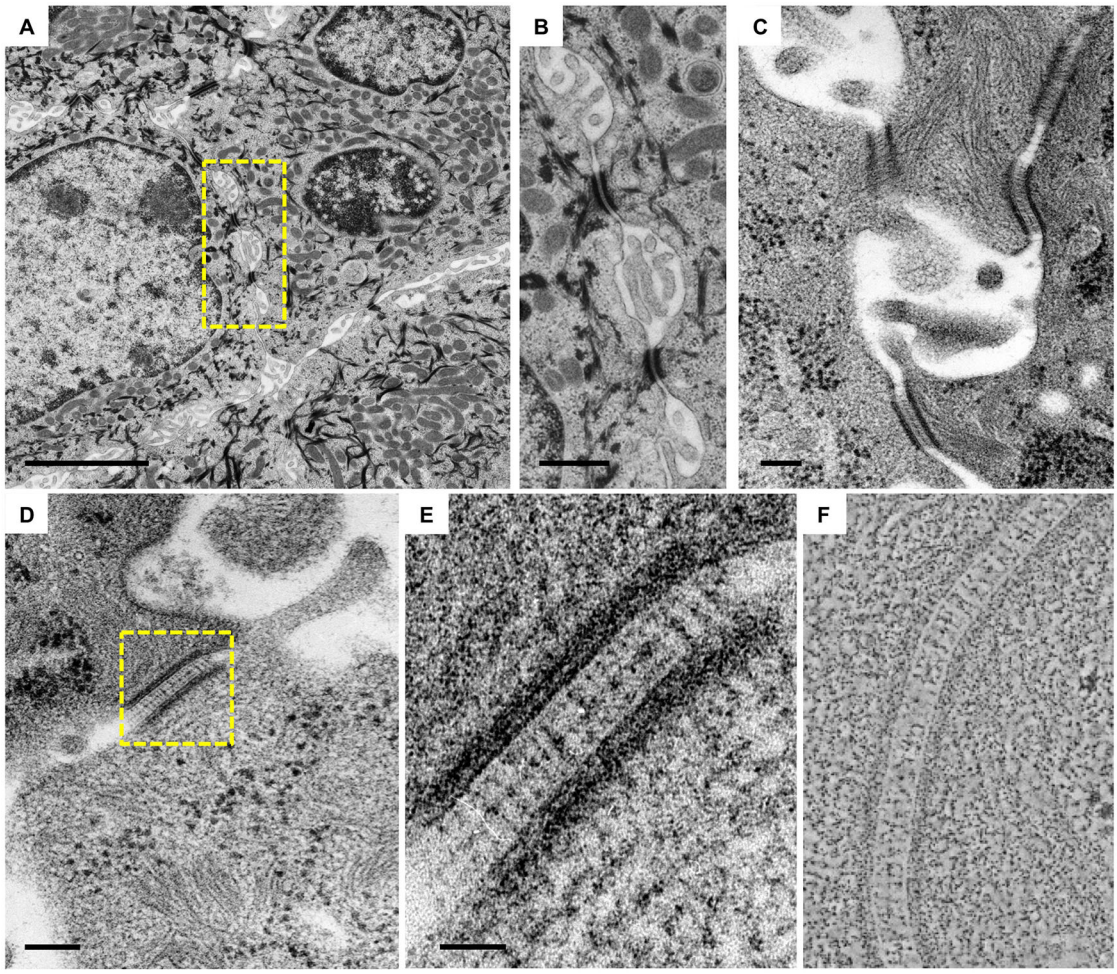

Fig. 2. Basolateral desmosomes are flanked by membrane protrusions in acini that have been optimally preserved. (A) Thin section TEM analysis revealed that the intercellular space contains copious membrane protrusions. (B) Boxed region of A, this region displayed a complex mix of protrusions that are adjacent to spot-like junctions. (C) The punctate cell–cell adhesion complexes that frame the membrane protrusions are likely to be desmosomes. (D) High-magnification view from thin section TEM analysis of the electron-dense plaques. (E) In the boxed region of D, the electron-dense plaques of the desmosome are apparent, and well-separated filaments spanned the gap between them. Using electron tomography (F), a single 1-nm slice through the tomogram affirmed that the gap between plaques spanned 30–35 nm and that the filaments between plaques were, on average, 5–10 nm thick; the midline of cadherin dimer overlap in the intercellular space could be visualized in the tomogram (F) and thin section TEM analyses (E). Scale bars: 5 µm (A); 1 µm (B); 100 nm (C); 100 nm (D); 30 nm (E).

lumen. It should be pointed out however that, based on studies of the mammary glands of virgin mice and mice in the early stages of pregnancy, highly ordered tight junctions and a completely closed lumen appear only on day 15 of pregnancy (Barcellos-Hoff et al., 1989; Pitelka et al., 1973), when components of other milk proteins such as whey acidic protein appear (Bissell and Ram, 1989; Chen and Bissell, 1989; Lin and Bissell, 1993).

Membrane protrusions in the intercellular space form an extensive 3D network

When imaging large areas, we found the internally located intercellular spaces to be continuous with the 3D ECM space without tight junctional complexes, which are needed to form a tight luminal seal (Fig. 3A,B). Many of the intercellular protrusions that resembled microvilli contained short randomly oriented thin filaments (Fig. 3C, arrows), consistent with actin filaments that are typically found in microvilli lining the luminal space in epithelial tissues. However, unlike typical microvilli, which given a certain cell type adopt a consistent shape and length within the same cell (Sauvanet et al., 2015), we found membrane protrusions of various lengths, some of which were branched, further indicating that their architecture could be more complex.

To address this complexity and obtain insight into their 3D architecture, we performed FIB-SEM imaging (Fig. 3D–F), which allows the 3D reconstruction of large cellular volumes at ∼10-nm resolution. FIB-SEM generates 3D data by cycling between back-scattered electron imaging of a sample block surface and focused ion beam ablation of the surface, iterating on this process thousands of times to sequentially cut through a volume of sample. Each slice or ablation of the specimen surface is tightly controlled to be a specific thickness, thus generating a defined *z*-dimension for the voxel size (i.e. the *z*-slice thickness for the FIB-SEM datasets in this manuscript are each 4 nm and thus provides a voxel dimension of 4 nm^3). Such images (a single 4-nm image from a stack is shown in Fig. 3D) can then be combined into a 3D volume, revealing the complexity of these membrane protrusions that can be traced in 3D through manual segmentation of each individual slice (Fig. 3E). The resulting 3D map shows that these membrane protrusions adopted a

Journal of Cell Science (2017) 130, 177-189 doi:10.1242/jcs.190967

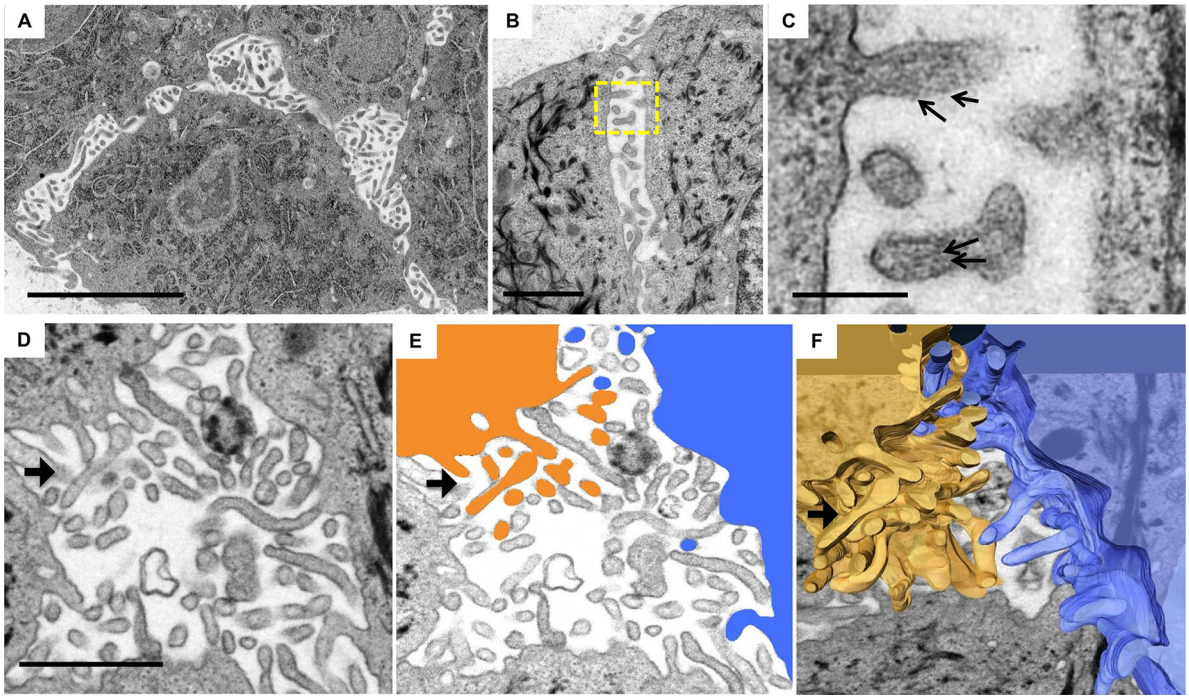

Fig. 3. Extensive membrane protrusions fill the intercellular space. (A,B) Thin section TEM revealed the 2D disorganization of membrane protrusions that fill the intercellular space. (C) Higher magnification of the protrusions in B revealed membrane-bound structures, which appeared to be randomly oriented. The protrusions were filled with cytoplasmic density and occasionally contained organized filaments (arrows). To further understand the full organization of these protrusions, FIB-SEM imaging and feature segmentation was performed (D–F, black arrows follow a single region for orientation). A representative single 4-nm slice of (D) the raw dataset and (E) colored masks of two cells manually segmented highlight protrusions in the single slice that connect back to their respective cytoplasms (orange, left cell; blue, right cell). (F) The whole segmented volume of cytoplasm and protrusions for the two masked cells in E revealed the complex and unexpected inter-connectivity between the protrusions of opposing cells. The 3D architecture displayed by membrane protrusions includes branched, looping and interwoven structures. Scale bars: 5 µm (A); 2 µm (B); 250 nm (C); 1 µm (D).

complex 3D architectural network of interacting membrane protrusions (Fig. 3F), similar to those found in mouse mammary epithelial cells in organotypic 3D culture undergoing branching morphogenesis (Ewald et al., 2012). The protrusions observed in three dimensions also branched often, folded back into the plasma membrane like ruffles, had bulges and uneven thickness, and were of differing lengths.

Nuclear invaginations in thin sections are 3D crevices and tunnels, as observed by performing FIB-SEM, STORM and confocal immunofluorescence microscopy

2D TEM and 3D FIB-SEM imaging of multiple S1 acini grown in 3D lrECM revealed deep invaginations of the nuclear membrane into the nucleus (TEM, Fig. 4A,B; FIB-S.E.M., Fig. 4C–F). These nuclear invaginations are known as type-II nucleoplasmic reticulum (Malhas et al., 2011; Malhas and Vaux, 2014). Some nucleoplasmic reticulum invaginations in S1 acini appeared to be rather wide (~300 nm) (Fig. 4A) and contained ~25–30-nm particles, which we interpret to be ribosomes (Fig. 4B). Inside the nucleus, sites of invaginations often displayed electron-dense heterochromatin in close proximity to the complexes that flanked the inner nuclear membrane and that spanned the inner and outer nuclear membrane, and thus are indicative of nuclear pore complexes (Fig. 4B). Note that owing to the specific sample preparation method chosen for the 2D TEM imaging, internal membranes showed low contrast (Giddings, 2003; McDonald and Morphew, 1993; Triffo et al., 2008). Also, owing to the difference in heavy metal staining needed to image samples with FIB-SEM, the texture of the chromatin within the nucleus appeared to be less heterogeneous in comparison to that upon staining for TEM (Fig. 4C–F).

Other nucleoplasmic reticulum invaginations appeared as narrow (~25–50 nm) clefts and often contained a thin filament ~30–40 nm in diameter in cross-sections near the base of the invagination deep inside the nucleus (left cell of Fig. 4C, left inset), which ran parallel to the cleft membranes without ever entering the nucleus (Fig. 4C–E, Movie 3). Likewise, the perpendicular longitudinal view resolved this filamentous structure as a fiber. Note the inserts providing close-up views of two filaments in two different cells recorded in cross-sectional and in longitudinal orientations, respectively (Fig. 4C). Another view of cross-section filaments in cells is shown in Fig. 4D. Here, three thin filaments can be observed within the nuclear invagination, with one being in very close proximity to the outer nuclear membrane (Fig. 4E). Fig. 4C–E are 4-nm 2D slices of 3D volumes imaged by using FIB-SEM. The narrow crevice-like nature of these invaginations became clearer upon 3D rendering of the segmented nuclear envelope that is depicted in Fig. 4F. Primary cilia and centrosomes were observed in four of the cells at the apical surface and away from the nucleus; further, Golgi that had been previously observed at distinctly apical locations in confocal microscopy and volume electron microscopy analyses were not observed to be exclusively located near to invaginations, thus indicating that these invaginations are unlikely to be traditional nuclear clefts (Fig. 1; Fig. S1 and Movie 3) (Bourgeois et al., 1979; Elkouby et al., 2016; Hulspas et al., 1994).

In order to confirm that these nuclear crevices were indeed nucleoplasmic reticulum invaginations in the nuclear envelope, we labeled S1 cells that had been grown in 2D culture with antibodies against the nuclear envelope protein lamin B1 and then imaged these cells using conventional confocal microscopy and 3D STORM, which allows protein localization in three dimensions at ~20-nm resolution

Journal of Cell Science (2017) 130, 177-189 doi:10.1242/jcs.190967

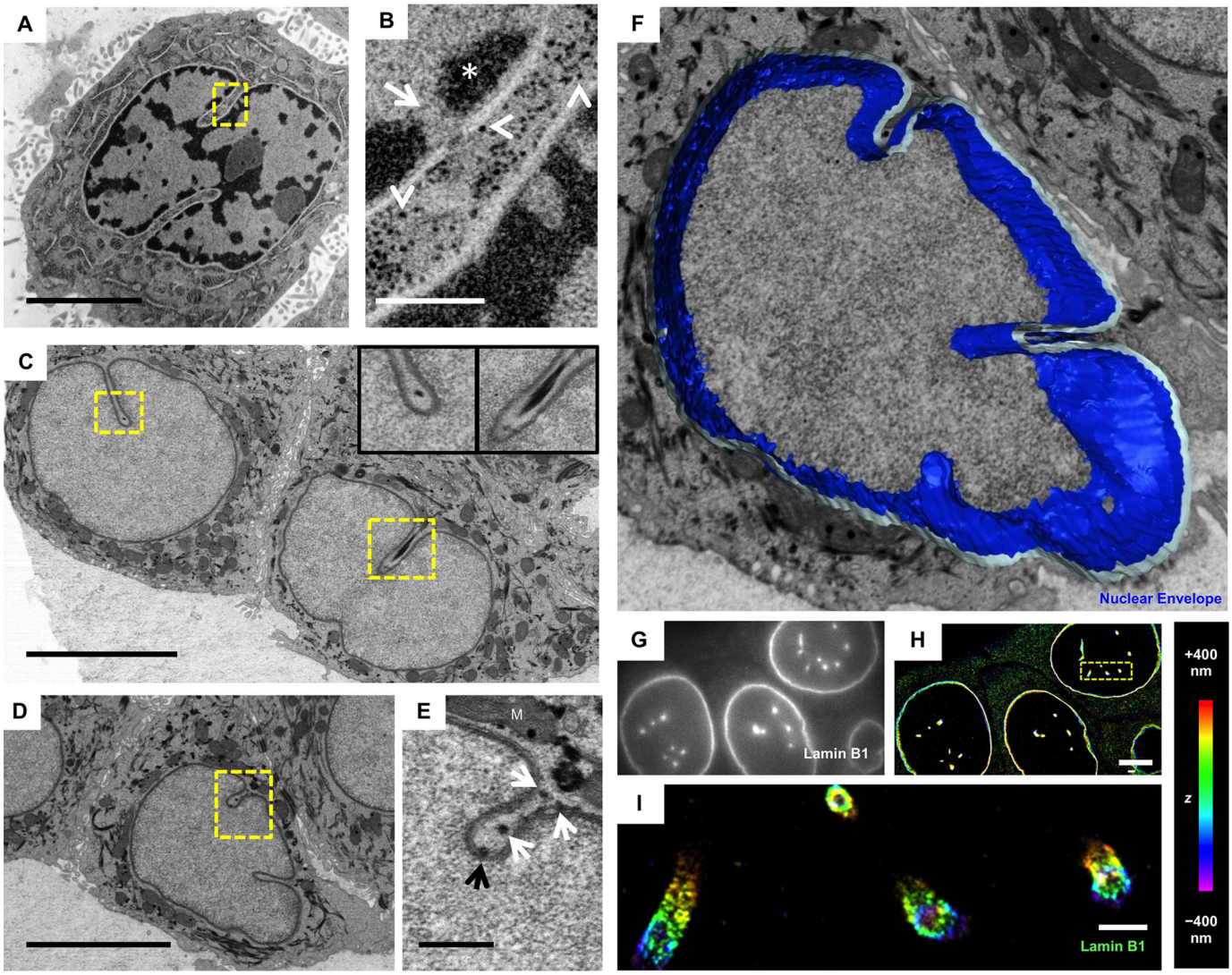

Fig. 4. Nuclear invaginations observed in thin sections are 3D tunnels and crevices, as shown by FIB-SEM and STORM. (A) In thin section TEM, large nuclear invaginations were observed, and (B, boxed region of A) when imaged at higher magnification, cytoplasmic material (ribosomes, arrow heads) and nuclear pores (arrow) were observed in the crevice, and heterochromatin (asterisk) was observed on either side of the nuclear pore. To more clearly understand the ultrastructure of these invaginations, (C–F) FIB-SEM imaging was performed. (C,D) Single 4-nm slices are shown from the volume dataset; (C) the insets demonstrate that a filamentous structure appears to track along the curvature of invagination of the nucleus – left inset, filament in cross-section and right inset, filament obliquely sliced. (E) Boxed region of D, multiple filaments (black and white arrows) were observed, with one making close contact to the nuclear envelope, which is likely to be a point of termination at the nuclear envelope (black arrow); a mitochondrion (M) is next to the nuclear crevice. (F) 3D rendering of the nuclear envelope (blue contour) demonstrated that the nuclear invaginations are crevices propagated across the surface of the nucleus. To determine whether these structures could be detected by using light microscopy, (G) epifluorescence and (H,I) STORM imaging were performed on S1 cells that had been immunolabeled for lamin B1. Again, nuclear invaginations were observed and had propagated into the nucleus over at least 600 nm, as shown in I. Position in the *z*-axis is represented by color from –400 nm (violet) to +400 nm (red). Scale bars: 5 µm (A); 500 nm (B); 5 µm (C); 5 µm (D); 500 nm (E); 5 µm (H); 500 nm (I).

(Huang et al., 2008; Rust et al., 2006). Although conventional confocal immunofluorescence microscopy showed a punctate signal for lamin B1 apparently residing inside the nuclear volume (Fig. 4G), STORM 3D imaging resolved these structures as hollow tubes that could be followed in 3D for over 600-nm in length (Fig. 4H,I). The hollow tubes revealed by 3D STORM analysis resembled the nuclear crevice invaginations revealed in electron micrographs. Note that the color coding reflects the position in the axial *z* direction.

Invaginations of the nuclear membrane in human breast epithelial cells

Electron microscopy analysis of normal human breast epithelium has consistently revealed that the nuclei of normal HMECs display type-II nucleoplasmic reticulum nuclear invaginations (Eyden et al., 2013; Lingle and Salisbury, 1999; Malhas et al., 2011; Ozzello, 1974; Stirling and Chandler, 1976; Tsuchiya and Li, 2005). We found that immunostaining of normal human breast tissue for lamin B1 illuminates the uneven topology of the nucleoplasmic reticulum of the nuclei of HMECs *in vivo* (Fig. 5A). Type-II nucleoplasmic reticulum is apparent in both mammary ductal and acinar cells (Fig. 5A,B; Movies 4 and 5), and in both myoepithelial cells and luminal epithelial cells, consistent with published electron microscopy data and our electron microscopy analysis of mouse mammary epithelial tissue (Fig. S2). Confocal stacks of lamin B1 staining illuminated nucleoplasmic reticulum invaginations in the *z*-plane (Fig. 5C). A nucleoplasmic reticulum invagination in an

Journal of Cell Science (2017) 130, 177-189 doi:10.1242/jcs.190967

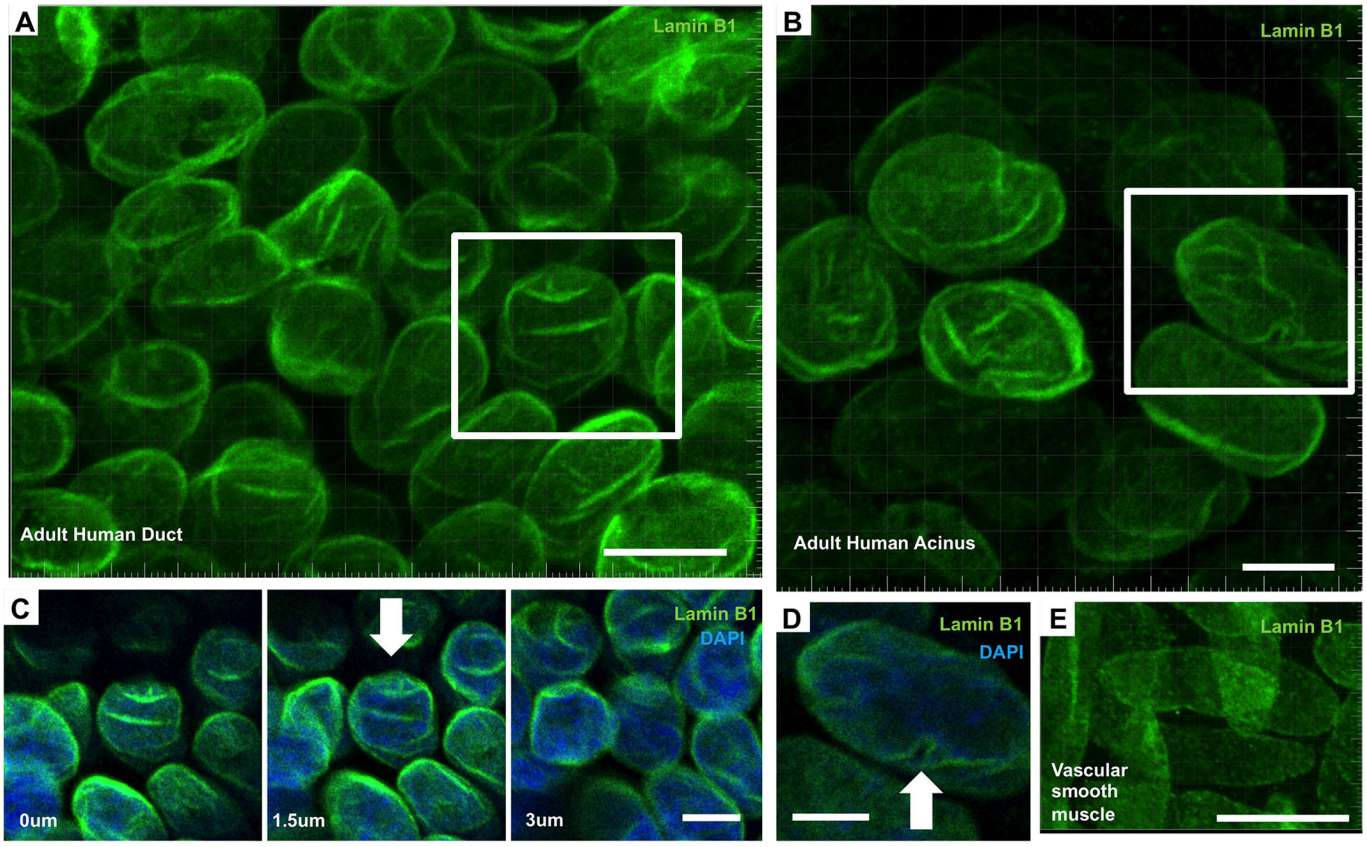

Fig. 5. Nuclear invaginations of the nucleoplasmic reticulum in normal human breast tissue. (A–E) Images of lamin B1 immunostaining in normal human mammary tissue. (A) Maximum intensity projections of mammary epithelial ductal and (B) acinar cells. Both areas have cells with uneven nuclear membranes, indicative of invaginations of the nucleoplasmic reticulum. (C) Three confocal slices of the ductal epithelium (white box) showing invaginations and uneven surface topology (white arrow). DAPI-stained nuclei are blue. Depths of the slices are given in the bottom left of the images. (D) Confocal slice of the acinar epithelium (white box) showing nuclear invagination (white arrow). DAPI-stained nuclei are blue. (E) Vascular smooth muscle from the same tissue section displaying convex nuclei that do not show nucleoplasmic reticulum invaginations. Scale bars: 5 µm (A); 5 µm (B); 3 µm (C); 3 µm (D); 10 µm (E).

acinar cell clearly revealed the uneven topology of the nucleus (Fig. 5D, arrow). The appearance of the nuclear membrane in cells from the same sample was strikingly different, lacking type-II nucleoplasmic reticulum, as shown with lamin B1 staining of vascular smooth muscle cells (Fig. 5E). This suggests that the unique shape of the nuclei, as influenced by the nucleoplasmic reticulum invaginations observed in mammary epithelium, is unlikely to be a preparation artifact.

Actin- and keratin-based cytoskeletal filaments inside nuclear tunnels form bridges to the nucleus and mechanically connect the outer nuclear envelope membrane with cell adhesion complexes

A dense cage of cytoskeletal elements surrounding the nucleus and extending out to cell–cell junctional complexes were observed in multiple 3D volume electron microscopy datasets. Cytoskeletal elements, furthermore, traversed nuclear tunnels formed by the nuclear envelope (Fig. 6). As shown in Fig. 6A, we found tunnels through the nucleus in the 3D FIB-SEM data sets (Movies 3 and 6). Such tunnel-like partitions of the nucleus were also observed in 2D TEM images (e.g. Fig. 1K–M; Movie 1), but these features could only be fully appreciated upon 3D FIB-SEM imaging (Fig. 6A–D; Movie 3). Close inspection of a filament in the nuclear tunnel (Fig. 6B) suggested that it could be an intermediate filament bundle based on its 3D morphology; however no conical bundles of similar size were observed in the cytoplasm, as demonstrated in the 3D rendering of the segmented filament network (Fig. 6C; Movie 6).

Interestingly, we noticed that the main thick cytoskeletal filament traversing a nuclear tunnel displayed a number of small branches, sometimes almost perpendicular to the main filament axis direction (Fig. 6C,D). We found that these small filaments terminated on the nuclear envelope membrane (Fig. 6D,E), suggesting a mechanical link between cell–cell adhesion sites and regions deep inside the nucleus through the intermediate filament network. Fig. 6F is a 3D rendering of both the cytoskeletal network as well as the nuclear membrane. Note that all 3D models are shown on top of a bottom 2D 4-nm slice of the 3D FIB-SEM volume (shown in grayscale) in order to provide adequate ultrastructural context. A scroll-through movie of the 3D volume and segmentation is provided (Movies 3 and 6).

We studied entire S1 acini at somewhat lower resolution using serial block face SEM imaging (SBF-SEM), which uses a diamond knife instead of an ion beam to trim and thus expose a new block surface for SEM imaging (Movie 7). Over the course of imaging multiple acini, we observed nuclear envelope folding and tunnels in a number of cells, thus confirming that the nucleoplasmic reticulum topology was present in a substantial proportion of cells (Movie 7, 8, 9). Given the novelty of these cytoskeletal transnuclear tunnels, we wanted to confirm these structures using more traditional approaches, such as immunofluorescence confocal microscopy for lamin B1. We imaged 15 acini totaling 203 cells (from two

Journal of Cell Science (2017) 130, 177-189 doi:10.1242/jcs.190967

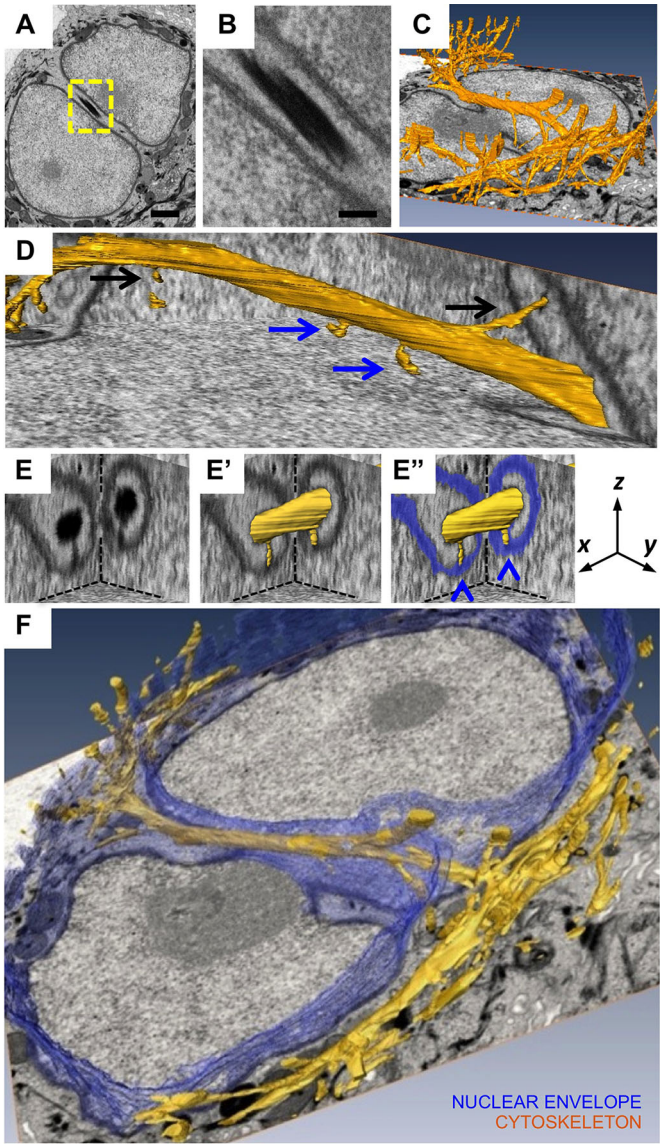

Fig. 6. 3D cytoskeletal organization bridges the nuclear tunnels. (A–F) A FIB-SEM dataset displaying a nuclear tunnel with a traversing thick cytoskeletal filament. (A) A single 4-nm slice of a FIB-SEM image in which the electron density of the tunneling filament is observed and (B, boxed region in A) a close-up view of the filament, which reveals the density and wispy texture. (C) The filament, rendered in 3D from the volume electron microscopy FIB-SEM dataset, linking into the cytoarchitecture of the cell, most of which is made up of intermediate filaments. Filament, continuous with cytoskeleton, rendered in yellow. (D) View of the nucleus-spanning region of the filament in which branches are observed terminating at the nuclear envelope (blue and black arrows). (E–E″) Cartesian coordinate cross-sections through the filament, revealing two separate branches (blue arrows in D) coming off the filament, with (E) the original electron microscopy density or (E′, yellow) as segmented volumes with the branches connected directly to the nuclear envelope (E″, nuclear envelope in blue). (F) The cytoskeleton (yellow) segmented and overlaid with the nuclear envelope (blue), rendered transparent, demonstrating that the nuclear envelope completely encloses the cytoskeletal filament. Scale bars: 1 µm (A); 0.25 µm (B).

experiments), and counted the cells that showed nuclear envelope folding and tunnels (Fig. 7A; Movie 10). We found that all studied cells displayed nuclear membrane wrinkling and that 51% of the cells studied displayed one or more nuclear tunnels, defined as a lamin B1 nuclear membrane signal traversing the nucleus, thus indicating tunneling of the nuclear membrane through the nucleus (Fig. 7B arrows, C, Movies 11, 12, 13). In addition, we quantified tunnels by performing volume electron microscopy and found that in 32 cells from five acini examined, 10 cells (31.25%) displayed one or more nuclear tunnels (Fig. 7C; Movie 7). By using both volume electron microscopy and confocal microscopy, we found that ∼9% of cells had two tunnels, and 2–3% displayed three or more tunnels that traversed the nucleus (Fig. 7C; Movie 14). Furthermore, live-cell imaging of HMT-3522-S1 cells using lipophilic membrane dyes showed nuclear membrane that clearly traversed the nucleus, thus demonstrating that the tunnels observed are not an artifact of fixation or processing during the sample preparation for electron microscopy and immunofluorescence analyses (Fig. S3; Movie 15).

Based on the dimensions of the cytoskeletal fibers observed in nuclear tunnels, we suspected that the fibers observed in nuclear tunnels contained intermediate filaments, although they could also contain actin. In order to address whether these cytoskeletal elements were actin- and/or cytokeratin-based, we performed 3D STORM imaging on S1 cells labeled with either phalloidin–Alexa-Fluor-647 or with a pan-cytokeratin primary antibody and an Alexa-Fluor-647-conjugated secondary antibody. Surprisingly, we found evidence for the presence of both actin (Fig. 7D) and cytokeratins (Fig. 7E) in the cytoskeletal filaments traversing the nucleus, which were also detectable in conventional fluorescence imaging (see Fig. 7D,E inserts, respectively) but became much more prominent upon 3D STORM imaging.

SUN-domain proteins have been recognized widely as mechanical linkers between the cytoskeleton and the nuclear envelope (Lombardi et al., 2011; Starr and Fridolfsson, 2010; Tapley and Starr, 2013; Tzur et al., 2006). Mediated by KASH proteins and nesprins, SUN-domain proteins act as anchors within the nuclear membrane that mechanically couple the nucleus with cytoskeletal actin and intermediate filaments (Tzur et al., 2006). Recent work has shown that SUN proteins play a crucial role in transmitting mechanical stimuli from the extracellular environment into intracellular chemical signals, including those affecting cell polarization (Lombardi et al., 2011).

We hypothesized that SUN proteins can act as a linker between deep nuclear invaginations and the cytoskeleton, which in turn links to desmosomes and hemidesmosomes, thus transducing forces between neighboring cells in acini deep into the nucleus. By performing two-color STORM imaging of SUN-1 and cytokeratins, we found that SUN-1 was concentrated at the nuclear tunnels and invaginations, and encircled the cytokeratin filaments that tunneled into and through the nucleus (Fig. 7F–H). This result indicates that the cytoskeletal filaments that we detected by performing electron microscopy and 3D STORM do not merely tunnel into and traverse the nucleus, but rather directly link the nuclear membrane deep within invaginations to the external cellular environment. We speculate that the unique spatial distribution of SUN and cytoskeletal proteins deep within the nucleus allows for extracellular mechanical signals to strongly influence the collective polarization of cellular units within acini.

DISCUSSION

In this work, we investigated, at ultra-high resolution, the structure of cells organized into tissue. We chose to image the HMT-3522 S1 cell line, which is part of a well-studied *in vitro* model of breast cancer progression (Briand et al., 1996, 1987; Petersen et al., 1992; Weaver et al., 1997). The S1 non-malignant HMEC cell line recapitulates several important aspects of the mammary gland *in vivo*, such as growth arrest

Journal of Cell Science (2017) 130, 177-189 doi:10.1242/jcs.190967

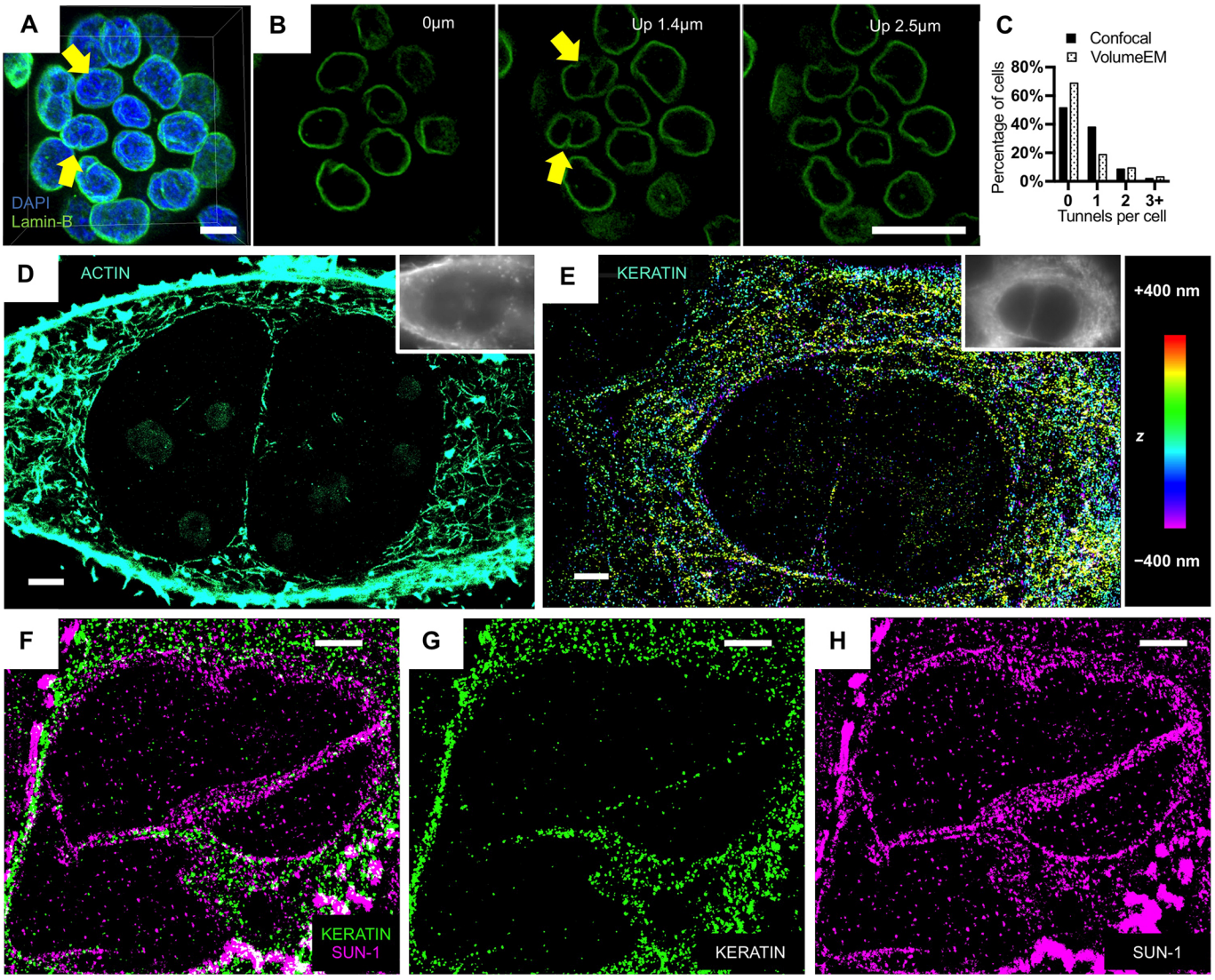

Fig. 7. The 3D cytoskeletal organization bridges the nuclear tunnels and contains both actin and keratin. (A) Confocal imaging of a growth-arrested acini, labeled for lamin B1 and DAPI. All nuclei display a wrinkled envelope. Arrows indicate sites of nuclear tunnels. (B) A step-wise progression through the lamin B1 staining highlights nuclear tunnels in multiple nuclei (B, arrows). (C) Quantification of the number of nuclear tunnels per cell in confocal stacks (solid bars) and volume electron microscopy (EM) analyses (open dotted bars). (D) 2D STORM and epifluorescence (inset) image of actin filaments labeled by phalloidin, with the focal plane at the center of the nucleus. The image shows actin filaments going through the center of the nucleus from a side-view perspective, as well as small patches of actin filaments that are likely to have entered the focal plane through invaginations of the nuclear envelope. (E) 3D STORM and epifluorescence (inset) images of cytokeratin in another sample, showing keratin filaments going through the center of the nucleus from a side-view perspective. Color was used to present the height (*z*) information according to the color scale bar, with violet being closest to the coverslip and red being farthest away. (F) Two-color STORM image of cytokeratin (green) and SUN-1 (magenta); the focal plane is at the center of the nucleus. (G,H) The separated cytokeratin and SUN-1 channels, respectively. SUN-1 is concentrated at nuclear tunnels and invaginations and encircles keratin filaments that traverse the nuclear space. Scale bars: 5 µm (A); 10 µm (B); 2 µm (D–H).

and aspects of polarity, simultaneously affording reproducibility and control that is not possible with native tissue. Furthermore, the relative small size and yet multicellular complexity of the acinus makes it an ideal model system for high-resolution 2D and 3D analysis.

We identified a number of features of growth-arrested polarized cultures that have not previously been associated with normal function and, for the first time, imaged the physical structure of the cytoskeletal linkage from the desmosomes and hemidesmosomes to the nuclear membrane. Using high-resolution electron microscopy imaging technologies, including 2D TEM, 3D electron tomography and FIB-SEM, along with optical microscopy techniques, including epifluorescence microscopy, confocal microscopy and 3D STORM, we were able to image the architectural features of growth-arrested acinar cultures at multiple scales and unprecedented resolution.

By using immunofluorescence analysis, we found that growth-arrested S1 structures displayed a number of important features of luminal epithelial acini *in vivo*, including localization of both basal and apical polarity markers both in this and our previous work. By integrating multiple modes of microscopy, we constructed a much higher-resolution view of the 3D architecture of growth-arrested acinus-like structures in the S1 breast epithelial cell line. We found aspects of basal polarity and the presence of an extensive membrane protrusion network, which might allow neighboring cells to maximize cell–cell contact areas without generating junctional

Journal of Cell Science (2017) 130, 177-189 doi:10.1242/jcs.190967

commitments. Although the structures could undergo growth arrest, we did not observe tight junctions or an organized lumen.

Using large 3D volume electron microscopy techniques, we observed deep invaginations into the nucleus, some of which completely traversed the nucleus. We observed that such tunnels frequently enclosed cytoskeletal elements, which we identified as both actin and cytokeratin intermediate filaments. FIB-SEM 3D analysis revealed the cytoskeletal filaments end at and possibly connect to the nuclear envelope without entering directly into the nucleus space. Our observations are consistent with previous work that has suggested that cytoskeletal elements in nuclear invaginations could be sites that are rich in linker of nucleoskeleton and cytoskeleton (LINC) complexes – i.e. bridges between the cytoskeleton and chromatin (Versaevel et al., 2014).

An important aspect of this work is our demonstration that the cytoskeletal connection from desmosomes and hemidesmosomes to the nucleus can take on unexpected and surprising shapes. A few papers have described previously a mechanical linkage between the plasma membrane and the nuclear membrane (Kim and Wirtz, 2015; Lombardi et al., 2011; Maniotis et al., 1997). Our finding of an intermediate filament cage surrounding the nucleus, and occasionally passing into the nuclear space through invaginations or tunnels in the nucleus, suggests a unique mechanical coupling between receptors on the plasma membrane and the nucleus that have not been found in previous work in mesenchymal-type cells cultured on rigid substrata, thus highlighting the power of the type of imaging that we've undertaken. Furthermore, two-color STORM imaging demonstrates that nuclear membrane linkers, such as SUN-1, can be observed in both the nuclear periphery and nuclear tunnels. Reports of nuclear invaginations have been in the literature for a long time (for review, see Malhas et al., 2011); however, the reason behind why nuclei in epithelial cells have folds and invaginations has not been well understood, and we believe that in this work we have provided a possible explanation.

We submit that our findings of nuclear invaginations that often contain cytoskeletal filaments, linked to the nuclear envelope, suggest a direct link between regions deep inside the nuclei and cell–cell and/or cell–ECM adhesion sites, which would allow mechanical ECM signaling to the nucleus and vice versa.

We further propose that integrated bioimaging is uniquely suitable to the study of other complex systems at different scales and resolution with multi-modal imaging and subsequent data integration at the model level. Having studied the HMT-3522-S1 cells in such detail, we are now ready to perform a comparative study between 2D and 3D cultures and tissues *in vivo* for the presence of the intriguing structures studied here in order to understand their functional significance.

MATERIALS AND METHODS

HMT-3522 cell culture

2D culture

HMT-3522-S1 and HMT-3522-T4-2 mammary epithelial cells were grown as previously described (Briand et al., 1996, 1987; Petersen et al., 1992; Weaver et al., 1997). Cells were routinely tested for contamination with the Lonza MycoAlert Assay.

3D culture

S1 cells grown in 2D culture were trypsinized and plated for 3D culture at 0.8 million cells per ml of lrECM (Matrigel) inside lrECM. Each assay comprised 2.4×10^5 S1 cells resuspended into 300 µl of lrECM and pipetted into a 4-well Nunc plate. Matrigel was allowed to polymerize, 500 µl of H14 medium was added, and assays were cultured at 37°C under a humidified atmosphere with 5% CO_2. Cultures were subsequently fed every 2–3 days, EGF was withdrawn from the medium at day 7, and acini were harvested at day 10.

Human breast tissue

Human breast tissue from reduction mammoplasty procedures was collected in compliance with relevant ethical regulations and approved by the Lawrence Berkeley National Laboratory Human Subjects Committee. Informed consent was obtained from all subjects.

Mouse mammary tissue

4th inguinal mammary glands were collected from three-week-old female C57BL/6 mice (*Mus musculus*) and processed for electron microscopy analysis, as described below. All tissues were collected in compliance with relevant ethical regulations and approved by the Lawrence Berkeley National Laboratory Animal Wellness Research Committee.

Immunofluorescence analysis

30-µm sections of optimal cutting temperature compound (O.C.T.)-embedded human breast tissue from reduction mammoplasty procedures or day-10 HMT-3522-S1 acini were immunostained as follows: S1 acini were harvested from 3D lrECM cultures either by pipetting the lrECM+acini directly onto a glass slide or by partially digesting the lrECM with a mixture of ice cold PBS+5 mM EDTA for 15–30 min. S1 acini or human tissue sections were fixed in 4% paraformaldehyde for 20 min at room temperature or fixed in 1:1 methanol:acetone for 20 min at −20°C. Slides were blocked in 10% goat serum in immunofluorescence buffer (see Lee et al., 2007) with anti-mouse IgG Fab fragments (1:250 dilution; BD Biosciences, 553998). Primary antibody was applied in blocking solution overnight at 4°C. Slides were washed three times for 2 h in immunofluorescence buffer. Secondary antibody was applied overnight at 4°C. Slides were washed three times for 2 h in immunofluorescence buffer and DAPI was applied. Acini were imaged on a Zeiss LSM 710 laser scanning confocal microscope equipped with a 100×1.4 NA objective and 405- and 488-nm laser lines. The pinhole was set to 1 AU for all experiments. Data was acquired and analyzed with Zen software or a Zeiss Axioskop Imaging platform with SPOT Basic software. Samples were stained with Alexa-Fluor-546–phalloidin (Invitrogen A12379, 1:200) to detect F-actin or with the following: rat anti-α6 integrin clone GoH3 (BD Pharmingen 555734, 1:300), rabbit anti-ZO-1 (Life Technologies 61-7300, 1:100), rabbit anti-lamin-B1 (Abcam ab16048, 1:500), rabbit anti-GM130 (Cell Signaling Technology 12480; 1:3000) and β-catenin (BD 610154, 1:200) antibodies. Alexa-Fluor-488-conjugated secondary antibodies (at 5 µg ml^{-1}) were used to label the primary antibodies.

EdU staining

S1 cells were grown in 3D lrECM culture for 10 days, on day 7, EGF was withdrawn from the medium and 24 h before harvest, EdU was added (5 µM). Tumorigenic HMT-3522-T4-2 cells were grown in 2D culture and labeled with EdU (5 µM) for 24 h. EdU incorporation was detected with the Click-iT EdU Alexa-Fluor-488 Imaging Kit (Invitrogen, C10337). Cells were counterstained with DAPI, and proliferation was determined by counting EdU-positive cells and total cells.

High-pressure freezing with freeze substitution

HMEC acini, unfixed in Matrigel, were placed in 1-mm wide by 200-µm deep aluminum freezing hats, and cryoprotected in 20% bovine albumin for freezing. The acini were then cryo-immobilized using a BAL-TEC HPM-010 high-pressure freezer (BAL-TEC, Inc., Carlsbad, CA). The samples that had been left unfixed before HPF were placed in freeze-substitution medium made up of 1% osmium tetroxide, 0.1% uranyl acetate and 5% ddH_2O in acetone. All samples were freeze-substituted, either by using a Leica AFS2 (Leica Microsystems, Wetzlar, Germany) following a previously described protocol (McDonald et al., 2007) or by super quick freeze substitution (McDonald and Webb, 2011). Following freeze-substitution, the acini samples were rinsed in pure acetone and then progressively infiltrated with an epon-araldite resin (McDonald and Müller-Reichert, 2002). Samples were flat or thin embedded before being polymerized overnight at 60°C (Muller-Reichert et al., 2003).

Journal of Cell Science (2017) 130, 177-189 doi:10.1242/jcs.190967

Volume electron microscopy sample preparation

HMEC acini that had been embedded within Matrigel were chemically fixed with electron-microscopy-grade 2% paraformaldehyde and 0.5% glutaraldehyde. The acini were stained by using an osmium-thiocarbohydrazide-osmium (OTO) method (Friedman and Ellisman, 1981; Willingham and Rutherford, 1984) in combination with microwave-assisted processing, followed by HPF-FS, as previous described (Ewald et al., 2012). Briefly, samples were subjected to HPF as described above and freeze-substituted with 4% osmium tetroxide, 0.1% uranyl acetate and 5% ddH_2O in acetone; they were then flat embedded and polymerized in hard epon resin.

Transmission electron microscopy

70–100-nm sections were collected on formvar-coated grids using a Reichert UltracutE ultramicrotome (Leica Microsystems, Germany). For serial section TEM, 100-nm sections were collected in ribbons of ∼five sections upon each grid to preserve the order and orientation of the sectioned material. Sections were post-stained using 2% uranyl acetate in 70% methanol followed by Reynold's lead citrate. The sections were imaged in an FEI Tecnai 12 transmission electron microscope (FEI, Hillsboro, OR) operated at 120 kV. Images were recorded using a Gatan CCD with Digital Micrograph software (Gatan Inc., Pleasanton, CA). ImageJ software (Abràmoff et al., 2004) and Adobe Photoshop CS4 (Adobe Systems Inc., San Jose, CA) were used for further image processing and for the registration of the serial section images for 3D analysis.

Volume electron microscopy imaging

For FIB-SEM, resin-embedded samples were polished with a dry diamond knife tool to expose the area of interest on both the top and one side of the block and then mounted to a 45° pre-tilt SEM stub using colloidal silver paint. Milling and imaging of the block was performed on a FEI Helios Nanolab 650 Dual Beam FIB with Slice and View software (FEI, Hillsboro, OR). 4000 by 6000 pixel images were collected with an Elstar in-lens BSE detector at 2 kV with a horizontal field width of 23 µm at a working distance of 2.46 mm; FIB milling was performed at 77 pA to generate a *z* dimension step size of 4 nm – 1200 total slices for a complete depth of 4.5 µm. Owing to errors with the Slice and View software, the FIB-SEM run was stopped and had to be restarted multiple times, thus there are some gaps in the entire dataset. For SBF-S.E.M. analysis, acini that had been embedded in resin were mounted onto an aluminum pin with a cyanoacrylate adhesive and loaded into a sample holder for the Gatan 3View system (Gatan Inc., Pleasanton, CA). Serial block face SEM was performed as previously described (Denk and Horstmann, 2004). SBF-SEM data were collected using a 3View system mounted on a FEI Quanta 600 FEG scanning electron microscope; serial images were 4000 by 4000 pixels and acquired at 5 kV; *z*-dimension slices of 50 nm. Volume representations and manual segmentations of the volume electron microscopy datasets were performed using FEI Amira software (FEI, Hillsboro, OR).

Electron tomography

For Electron tomography analysis, thin sections (100 nm) were imaged in a FEI Tecnai F30 microscope operating at 300 kV (Boulder Laboratory for 3D Electron Microscopy of Cells, University of Colorado). Binned 2000 by 2000, tilt series were collected on 4000 by 4000 pixel charge-coupled-device Gatan camera (Gatan, Inc., Pleasanton, CA) every 1° from 70° to −70°, using the UCSF tomography software (http://www.msg.ucsf.edu/Tomography/tomography_main.html) or SerialEM software package (http://bio3d.colorado.edu/SerialEM/). The nominal setting of defocus was 1 µm, and the pixel size of the data corresponded to 1 nm. Series were aligned with the help of either 10-nm or 15-nm gold fiducial markers (BBI Research, Inc., WI), and reconstructed in 3D by using the IMOD software package (http://bio3d.colorado.edu/imod/).

Immunofluorescence labeling for STORM imaging

S1 cells were cultured on #1.5 glass coverslips (12 mm diameter), as described above for 2D cell culture. For experiments aimed at visualizing the actin cytoskeleton, cells were initially fixed and extracted for 1 min with a solution of 0.3% (v/v) glutaraldehyde and 0.25% (v/v) Triton X-100 in cytoskeleton buffer (see Xu et al., 2012), and then post-fixed for 20 min in 2% (v/v) glutaraldehyde in cytoskeleton buffer (Small et al., 1999; Svitkina, 2007; Xu et al., 2012). For experiments visualizing pan-cytokeratins, cells were fixed for 15 min in ice-cold methanol. For immunofluorescence labeling, cells were blocked with a solution of 3% bovine serum albumin and 0.1% Triton X-100 in PBS, and then stained with primary and secondary antibodies. The primary antibodies used were mouse anti-cytokeratin (a pan antibody detecting cytokeratins 4,5,6,8,10,13,18) (Cell Signaling Technologies 4545P; 1:20), rabbit anti-lamin B1 (Abcam ab16048; 1:400) and rabbit anti-SUN1 (GeneTex GTX63537; 1:400) antibodies. Alexa-Fluor-647-conjugated secondary antibodies (at 5 µg ml^{-1}) were used to label primary antibodies for single color experiments. For two-color experiments, Alexa-Fluor-647-conjugated secondary antibodies (at 5 µg ml^{-1}) were used to label pan-cytokeratin primary antibodies and CF568-conjugated secondary antibodies (at 5 µg ml^{-1}) were used to label primary antibodies against SUN1. For fluorescent labeling of actin filaments, samples were incubated (Xu et al., 2012) with Alexa-Fluor-647-conjugated phalloidin (Invitrogen A22287) at ∼0.4 µM.

STORM imaging

3D STORM imaging (Huang et al., 2008; Rust et al., 2006) was performed on a home-built setup based on a Nikon Eclipse Ti-U inverted optical microscope using an oil immersion objective (Nikon CFI Plan Apochromat λ 100×, NA 1.45). Lasers at 647 nm (MPB Communications), 560 nm (MPB Communications) and 405 nm (Coherent) were coupled into an optical fiber after an acousto-optic tunable filter and then introduced into the sample through the back focal plane of the microscope. Using a translation stage, the laser beams were shifted toward the edge of the objective so that emerging light reached the sample at incidence angles slightly smaller than the critical angle of the glass-water interface. Continuous illumination of 647-nm laser (∼2 kW cm^{-2}; for Alexa-Fluor-647) or of a 560-nm laser (∼2 kW cm^{-2}; for CF568) was used to excite fluorescence from labeled dye molecules and to switch them into the dark state. Concurrent illumination of the 405-nm laser was used to reactivate the fluorophores to the emitting state. The power of the 405-nm laser (typical range 0-1 W cm^{-2}) was adjusted during image acquisition so that at any given instance, only a small optically resolvable fraction of the fluorophores in the sample were in the emitting state. For 3D STORM imaging, a cylindrical lens was inserted into the imaging path so that images of single molecules were elongated in the *x* and *y* axes for molecules on the proximal and distal sides of the focal plane (relative to the objective), respectively (Huang et al., 2008). The imaging buffer was as described previously (Xu et al., 2012).

Acknowledgements

We thank Dr Kent McDonald (University of California Berkeley Electron Microscopy Lab) for his advice and assistance in electron microscopy sample preparation. We thank Dr Jessie K. Lee, Dr Melissa J. Perez, Kester Coutinho, Michelle Lam and Polly Huang for their assistance with electron microscopy specimen preparation and screening. We thank Dr Jessica Riesterer (FEI, Inc.) for invaluable assistance with FIB-SEM data collection. We thank Dr Chris Booth (Gatan, Inc.) and Joel Mancuso (Gatan, Inc.) for their advice in sample preparation and SBF-SEM data collection. We thank Eva Lee, Sun-Young Moon Lee, William C. Hines, Chin Tien (Kate) Thi and Amirhossein Jaberi for assistance with HMEC and human breast tissue sample preparation. We thank Yennie Shyu for invaluable assistance with 2-color STORM data collection. Human tissue samples were provided by the Cooperative Human Tissue Network, a National Cancer Institute supported resource.

Competing interests

The authors declare no competing or financial interests.

Author contributions

Conception and design of research and writing were by M.A. and M.J.B.; K.X. conceived and designed STORM experiments; D.M.J. and J.L.I. performed most experiments and data analyses, and co-wrote the manuscript. M.W. performed STORM imaging, with help from H.H. and A.B.-C.; H.P. performed some electron microscopy and W.-T.T. visualized volume EM datasets; C.S.L. collected focused ion beam SEM data; C.R. performed confocal microscopy, live cell imaging and co-wrote the manuscript.

Funding
This research was supported by the National Institutes of Health (P01GM051487 to M.A., R01CA064786 to M.J.B., U54CA143836l to M.J.B.); the U.S. Department of Energy, Office of Biological and Environmental Research (DE-AC02-05CH11231 to M.J.B.); the U.S. Department of Defense, Breast Cancer Research Program (to M.J.B.); the Breast Cancer Research Foundation (to M.J.B.); the U.S. Department of Defense (BC133875 to C.R.); the L'Oreal USA for Women in Science Program (to C.R.); the National Science Foundation Graduate Research Fellowship (DGE 1106400 to M.W.); the School of Life Sciences, Peking University (to H.H.); and the Pew Charitable Trusts Biomedical Scholars program (to K.X.). Deposited in PMC for release after 12 months.

Data availability
All movies are available on figshare (https://dx.doi.org/10.6084/m9.figshare.c.2864557).

Supplementary information
Supplementary information available online at
http://jcs.biologists.org/lookup/doi/10.1242/jcs.190967.supplemental

References
Abràmoff, M. D., Magalhães, P. J. and Ram, S. J. (2004). Image processing with ImageJ. *Biophotonics Int.* **11**, 36-42.
Al-Amoudi, A., Díez, D. C., Betts, M. J. and Frangakis, A. S. (2007). The molecular architecture of cadherins in native epidermal desmosomes. *Nature* **450**, 832-837.
Barcellos-Hoff, M. H., Aggeler, J., Ram, T. G. and Bissell, M. J. (1989). Functional differentiation and alveolar morphogenesis of primary mammary cultures on reconstituted basement membrane. *Development* **105**, 223-235.
Becker-Weimann, S., Xiong, G., Furuta, S., Han, J., Kuhn, I., Akavia, U.-D., Pe'er, D., Bissell, M. J. and Xu, R. (2013). NFkB disrupts tissue polarity in 3D by preventing integration of microenvironmental signals. *Oncotarget* **4**, 2010-2020.
Bhat, R. and Bissell, M. J. (2014). Of plasticity and specificity: dialectics of the microenvironment and macroenvironment and the organ phenotype. *Wiley Interdiscip. Rev. Dev. Biol.* **3**, 147-163.
Bissell, M. J. and Hines, W. C. (2011). Why don't we get more cancer? A proposed role of the microenvironment in restraining cancer progression. *Nat. Med.* **17**, 320-329.
Bissell, M. J. and Labarge, M. A. (2005). Context, tissue plasticity, and cancer: are tumor stem cells also regulated by the microenvironment? *Cancer Cell* **7**, 17-23.
Bissell, M. J. and Ram, T. G. (1989). Regulation of functional cytodifferentiation and histogenesis in mammary epithelial cells: role of the extracellular matrix. *Environ. Health Perspect.* **80**, 61-70.
Bissell, M. J., Hall, H. G. and Parry, G. (1982). How does the extracellular matrix direct gene expression? *J. Theor. Biol.* **99**, 31-68.
Boudreau, N., Myers, C. and Bissell, M. J. (1995a). From laminin to lamin: regulation of tissue-specific gene expression by the ECM. *Trends Cell Biol.* **5**, 1-4.
Boudreau, N., Sympson, C. J., Werb, Z. and Bissell, M. J. (1995b). Suppression of ICE and apoptosis in mammary epithelial cells by extracellular matrix. *Science* **267**, 891-893.
Bourgeois, C. A., Hemon, D. and Bouteille, M. (1979). Structural relationship between the nucleolus and the nuclear envelope. *J. Ultrastruct. Res.* **68**, 328-340.
Briand, P., Petersen, O. W. and Van Deurs, B. (1987). A new diploid nontumorigenic human breast epithelial cell line isolated and propagated in chemically defined medium. *In Vitro Cell. Dev. Biol.* **23**, 181-188.
Briand, P., Nielsen, K. V., Madsen, M. W. and Petersen, O. W. (1996). Trisomy 7p and malignant transformation of human breast epithelial cells following epidermal growth factor withdrawal. *Cancer Res.* **56**, 2039-2044.
Bussard, K. M. and Smith, G. H. (2012). Human breast cancer cells are redirected to mammary epithelial cells upon interaction with the regenerating mammary gland microenvironment *in-vivo*. *PLoS ONE* **7**, e49221.
Chen, L. H. and Bissell, M. J. (1989). A novel regulatory mechanism for whey acidic protein gene expression. *Cell Regul.* **1**, 45-54.
Denk, W. and Horstmann, H. (2004). Serial block-face scanning electron microscopy to reconstruct three-dimensional tissue nanostructure. *PLoS Biol.* **2**, e329.
Elkouby, Y. M., Jamieson-Lucy, A. and Mullins, M. C. (2016). Oocyte polarization is coupled to the chromosomal bouquet, a conserved polarized nuclear configuration in meiosis. *PLoS Biol.* **14**, e1002335.
Ewald, A. J., Huebner, R. J., Palsdottir, H., Lee, J. K., Perez, M. J., Jorgens, D. M., Tauscher, A. N., Cheung, K. J., Werb, Z. and Auer, M. (2012). Mammary collective cell migration involves transient loss of epithelial features and individual cell migration within the epithelium. *J. Cell Sci.* **125**, 2638-2654.
Eyden, B., Banerjee, S. S., Ru, Y., Liberski, P. (2013). The Ultrastructure of Human Tumours: Applications in Diagnosis and Research. Berlin; Heidelberg: Springer.
Friedman, P. L. and Ellisman, M. H. (1981). Enhanced visualization of peripheral nerve and sensory receptors in the scanning electron microscope using cryofracture and osmium-thiocarbohydrazide-osmium impregnation. *J. Neurocytol.* **10**, 111-131.
Giddings, T. H. (2003). Freeze-substitution protocols for improved visualization of membranes in high-pressure frozen samples. *J. Microsc.* **212**, 53-61.
Hagios, C., Lochter, A. and Bissell, M. J. (1998). Tissue architecture: the ultimate regulator of epithelial function? *Philos. Trans. R. Soc. Lond. B Biol. Sci.* **353**, 857-870.
Hu, S., Chen, J., Butler, J. P. and Wang, N. (2005). Prestress mediates force propagation into the nucleus. *Biochem. Biophys. Res. Commun.* **329**, 423-428.
Huang, B., Wang, W. Q., Bates, M. and Zhuang, X. W. (2008). Three-dimensional super-resolution imaging by stochastic optical reconstruction microscopy. *Science* **319**, 810-813.
Hulspas, R., Houtsmuller, A. B., Bauman, J. G. J. and Nanninga, N. (1994). The centrosome moves out of a nuclear indentation in human lymphocytes upon activation. *Exp. Cell Res.* **215**, 28-32.
Kim, D.-H. and Wirtz, D. (2015). Cytoskeletal tension induces the polarized architecture of the nucleus. *Biomaterials* **48**, 161-172.
Lee, G. Y., Kenny, P. A., Lee, E. H. and Bissell, M. J. (2007). Three-dimensional culture models of normal and malignant breast epithelial cells. *Nat. Methods* **4**, 359-365.
Lin, C. Q. and Bissell, M. J. (1993). Multi-faceted regulation of cell differentiation by extracellular matrix. *FASEB J.* **7**, 737-743.
Lingle, W. L. and Salisbury, J. L. (1999). Altered centrosome structure is associated with abnormal mitoses in human breast tumors. *Am. J. Pathol.* **155**, 1941-1951.
Lombardi, M. L., Jaalouk, D. E., Shanahan, C. M., Burke, B., Roux, K. J. and Lammerding, J. (2011). The interaction between nesprins and sun proteins at the nuclear envelope is critical for force transmission between the nucleus and cytoskeleton. *J. Biol. Chem.* **286**, 26743-26753.
Malhas, A. N. and Vaux, D. J. (2014). Nuclear envelope invaginations and cancer. In *Cancer Biology and the Nuclear Envelope: Recent Advances May Elucidate Past Paradoxes* (ed. C. E. Schirmer and I. J. de las Heras), pp. 523-535. New York, NY: Springer.
Malhas, A., Goulbourne, C. and Vaux, D. J. (2011). The nucleoplasmic reticulum: form and function. *Trends Cell Biol.* **21**, 362-373.
Maniotis, A. J., Chen, C. S. and Ingber, D. E. (1997). Demonstration of mechanical connections between integrins, cytoskeletal filaments, and nucleoplasm that stabilize nuclear structure. *Proc. Natl. Acad. Sci. USA* **94**, 849-854.
McDonald, K. L. and Auer, M. (2006). High-pressure freezing, cellular tomography, and structural cell biology. *Biotechniques* **41**, 137-143.
McDonald, K. and Morphew, M. K. (1993). Improved preservation of ultrastructure in difficult-to-fix organisms by high pressure freezing and freeze substitution: I. Drosophila melanogaster and Strongylocentrotus purpuratus embryos. *Microsc. Res. Tech.* **24**, 465-473.
McDonald, K. and Müller-Reichert, T. (2002). Cryomethods for thin section electron microscopy. *Methods Enzymol.* **351**, 96-123.
McDonald, K. L. and Webb, R. I. (2011). Freeze substitution in 3 hours or less. *J. Microsc.* **243**, 227-233.
McDonald, K. L., Morphew, M., Verkade, P. and Müller-Reichert, T. (2007). Recent advances in high-pressure freezing: equipment- and specimen-loading methods. *Methods Mol. Biol.* **369**, 143-173.
Muller-Reichert, T., Hohenberg, H., O'Toole, E. T. and McDonald, K. (2003). Cryoimmobilization and three-dimensional visualization of C. elegans ultrastructure. *J. Microsc.* **212**, 71-80.
Osorio, D. S. and Gomes, E. R. (2014). Connecting the nucleus to the cytoskeleton for nuclear positioning and cell migration. *Adv. Exp. Med. Biol.* **773**, 505-520.
Ozzello, L. (1974). Electron microscopic study of functional and dysfunctional human mammary glands. *J. Invest. Dermatol.* **63**, 19-26.
Petersen, O. W., Ronnov-Jessen, L., Howlett, A. R. and Bissell, M. J. (1992). Interaction with basement membrane serves to rapidly distinguish growth and differentiation pattern of normal and malignant human breast epithelial cells. *Proc. Natl. Acad. Sci. USA* **89**, 9064-9068.
Pitelka, D. R., Hamamoto, S. T., Duafala, J. G. and Nemanic, M. K. (1973). Cell contacts in the mouse mammary gland: I. Normal gland in postnatal development and the secretory cycle. *J. Cell Biol.* **56**, 797-818.
Plachot, C., Chaboub, L. S., Adissu, H. A., Wang, L., Urazaev, A., Sturgis, J., Asem, E. K. and Lelièvre, S. A. (2009). Factors necessary to produce basoapical polarity in human glandular epithelium formed in conventional and high-throughput three-dimensional culture: example of the breast epithelium. *BMC Biol.* **7**, 77.
Rust, M. J., Bates, M. and Zhuang, X. W. (2006). Sub-diffraction-limit imaging by stochastic optical reconstruction microscopy (STORM). *Nat. Methods* **3**, 793-796.
Sauvanet, C., Wayt, J., Pelaseyed, T. and Bretscher, A. (2015). Structure, regulation, and functional diversity of microvilli on the apical domain of epithelial cells. *Annu. Rev. Cell Dev. Biol.* **31**, 593-621.
Small, J.-V., Rottner, K., Hahne, P. and Anderson, K. I. (1999). Visualising the actin cytoskeleton. *Microsc. Res. Tech.* **47**, 3-17.
Spencer, V. A., Costes, S., Inman, J. L., Xu, R., Chen, J., Hendzel, M. J. and Bissell, M. J. (2011). Depletion of nuclear actin is a key mediator of quiescence in epithelial cells. *J. Cell Sci.* **124**, 123-132.

Starr, D. A. and Fridolfsson, H. N. (2010). Interactions between nuclei and the cytoskeleton are mediated by SUN-KASH nuclear-envelope bridges. *Annu. Rev. Cell Dev. Biol.* **26**, 421-444.
Stirling, J. W. and Chandler, J. A. (1976). The fine structure of the normal, resting terminal ductal-lobular unit of the female breast. *Virchows Arch. A Pathol. Anat. Histol.* **372**, 205-226.
Svitkina, T. (2007). Electron microscopic analysis of the leading edge in migrating cells. *Methods Cell Biol.* **79**, 295-319.
Tanner, K., Mori, H., Mroue, R., Bruni-Cardoso, A. and Bissell, M. J. (2012). Coherent angular motion in the establishment of multicellular architecture of glandular tissues. *Proc. Natl. Acad. Sci. USA* **109**, 1973-1978.
Tapley, E. C. and Starr, D. A. (2013). Connecting the nucleus to the cytoskeleton by SUN–KASH bridges across the nuclear envelope. *Curr. Opin. Cell Biol.* **25**, 57-62.
Triffo, W. J., Palsdottir, H., McDonald, K. L., Lee, J. K., Inman, J. L., Bissell, M. J., Raphael, R. M. and Auer, M. (2008). Controlled microaspiration for high-pressure freezing: a new method for ultrastructural preservation of fragile and sparse tissues for TEM and electron tomography. *J. Microsc.* **230**, 278-287.
Tsuchiya, S.-i. and Li, F. (2005). Electron microscopic findings for diagnosis of breast lesions. *Med. Mol. Morphol.* **38**, 216-224.
Tzur, Y. B., Wilson, K. L. and Gruenbaum, Y. (2006). SUN-domain proteins: 'Velcro' that links the nucleoskeleton to the cytoskeleton. *Nat. Rev. Mol. Cell Biol.* **7**, 782-788.
Versaevel, M., Braquenier, J.-B., Riaz, M., Grevesse, T., Lantoine, J. and Gabriele, S. (2014). Super-resolution microscopy reveals LINC complex recruitment at nuclear indentation sites. *Sci. Rep.* **4**, 7362.
Weaver, V. M., Petersen, O. W., Wang, F., Larabell, C. A., Briand, P., Damsky, C. and Bissell, M. J. (1997). Reversion of the malignant phenotype of human breast cells in three-dimensional culture and in vivo by integrin blocking antibodies. *J. Cell Biol.* **137**, 231-245.
Weaver, V. M., Lelièvre, S., Lakins, J. N., Chrenek, M. A., Jones, J. C. R., Giancotti, F., Werb, Z. and Bissell, M. J. (2002). beta4 integrin-dependent formation of polarized three-dimensional architecture confers resistance to apoptosis in normal and malignant mammary epithelium. *Cancer Cell* **2**, 205-216.
Willingham, M. C. and Rutherford, A. V. (1984). The use of osmium-thiocarbohydrazide-osmium (OTO) and ferrocyanide-reduced osmium methods to enhance membrane contrast and preservation in cultured cells. *J. Histochem. Cytochem.* **32**, 455-460.
Xu, R., Nelson, C. M., Muschler, J. L., Veiseh, M., Vonderhaar, B. K. and Bissell, M. J. (2009). Sustained activation of STAT5 is essential for chromatin remodeling and maintenance of mammary-specific function. *J. Cell Biol.* **184**, 57-66.
Xu, R., Spencer, V. A., Groesser, D. L. and Bissell, M. J. (2010). Laminin regulates PI3K basal localization and activation to sustain STAT5 activation. *Cell Cycle* **9**, 4315-4322.
Xu, K., Babcock, H. P. and Zhuang, X. (2012). Dual-objective STORM reveals three-dimensional filament organization in the actin cytoskeleton. *Nat. Methods* **9**, 185-188.
Zhu, J., Xiong, G., Trinkle, C. and Xu, R. (2014). Integrated extracellular matrix signaling in mammary gland development and breast cancer progression. *Histol. Histopathol.* **29**, 1083-1092.

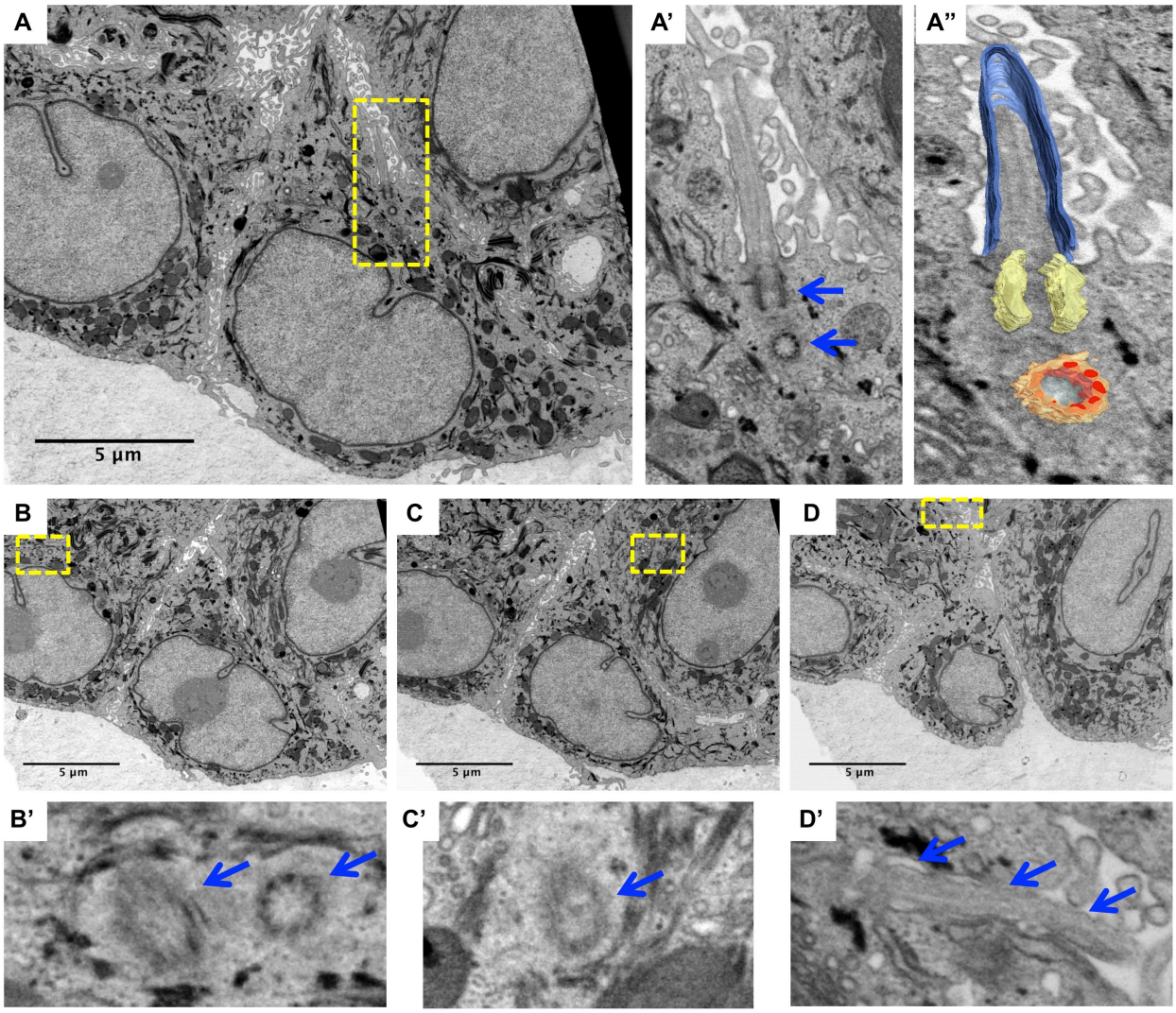

Figure S1. Apically oriented centrosomes and primary cilia in growth arrested acinus. (**A – D**) FIB-SEM dataset of growth arrested acinus in which upon the apical surface of four cells either primary cilia or centrioles are observed. (**A**) A single 4 nm slice of a FIB-SEM dataset, with (**A'**) primary cilium in apical location of central cell (blue arrows, basal body components). (**A"**) The primary cilium 3D structure displayed as a segmented volume (blue, cilium; collar, yellow; basal body, orange). (**B – B'**) Centrosome (blue arrows) of the left-most cell is visible. (**C – C'**) One basal body (blue arrow) in the right-most cell is observed. (**D – D'**) The primary cilium (blue arrows, defined upper length of the cilium) of the uppermost cell is visible.

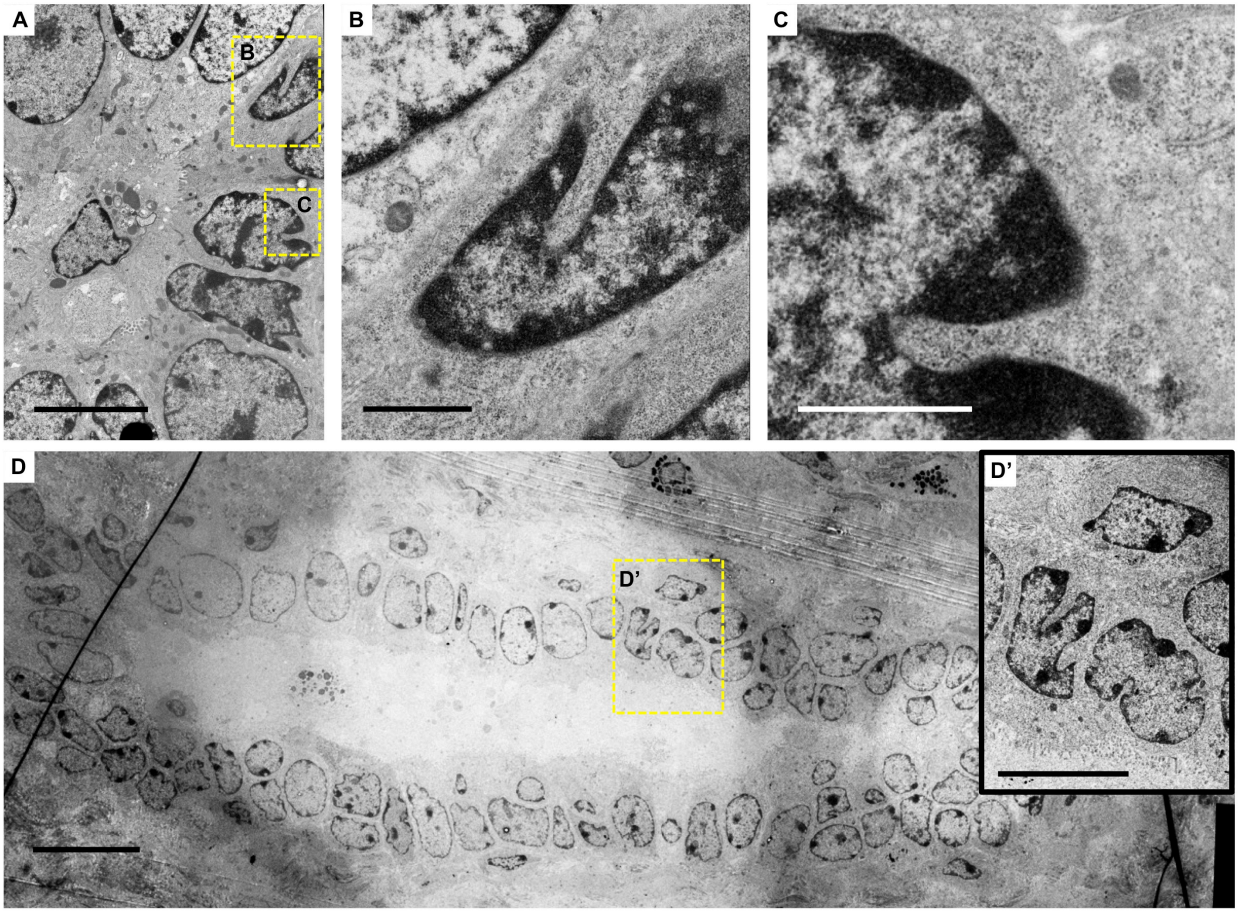

Figure S2. Wild type murine mammary gland TEM displays nucleoplasmic reticulum type II. (**A**) Cross-sectional view of the luminal space of a mammary duct in which two cells (**B**, **C**) have prominent type II nucleoplasmic reticula (NR). The cytoplasm is dense and filled with ribosomes in both cells. (**D**) Longitudinal view of a mammary duct with few cells (**D'**) displaying NR type II. Both (**A**) and (**D**) are TEM of 90 nm sections and indicate that NR can be difficult to properly visualize by 2D imaging alone. Scale bars for (**A**) 5 μm, (**B**) 1 μm, (**C**) 1 μm, (**D**) 10 μm, (**D'**) 5 μm.

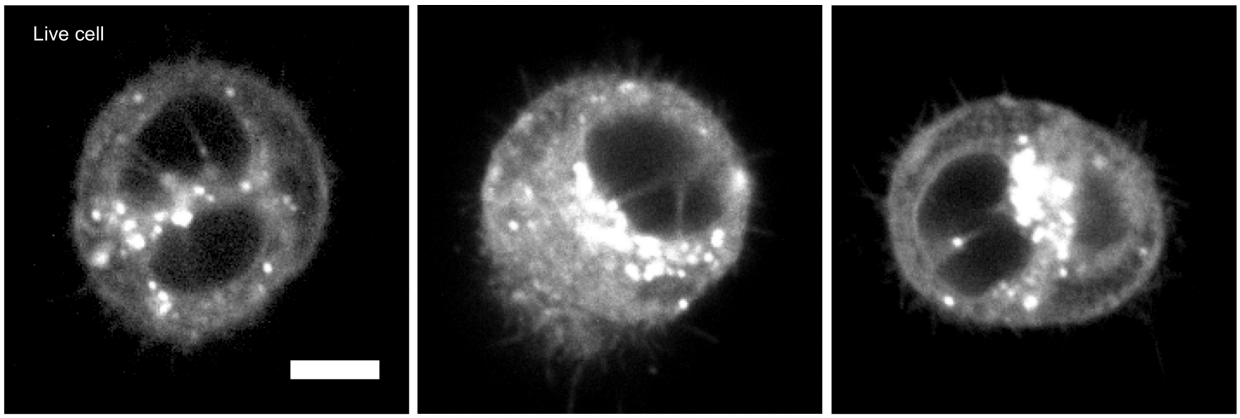

Figure S3. Live cell imaging of nuclear membrane in S1 cells. S1 cells were labeled with lipophilic membrane dye Vybrant Dil 24 hours prior to plating in 3D lrECM. Once plated in 3D lrECM cells were allowed to grow for 24 hours and then imaged. We find after 48 hours of labeling the Vybrant Dil membrane dye is internalized and labels internal membranes. Imaging of the dye shows multiple nuclear membrane tunnels traversing S1 nuclei. In some cases Golgi (brightly labeled organelles) appear to reside inside the tunnels. Scale bar 5 μm.

The full movie collection can be viewed on FigShare:
https://dx.doi.org/10.6084/m9.figshare.c.2864557

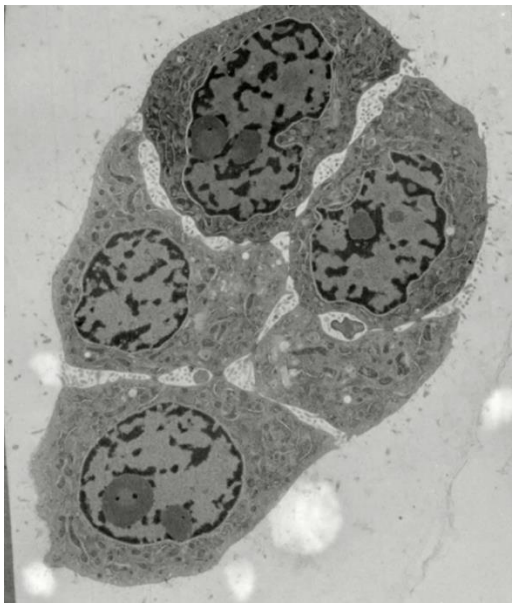

Movie 1: Serial section TEM of S1 acinus. Total depth of 2.2 micron of S1 acinus surveyed by serial section TEM. Twenty-two 100 nm thin sections sequentially cut and imaged by TEM. Images were overlaid with ImageJ (https://imagej.nih.gov/ij/). Serial sectioning provided 3-dimensional view across middle of an acinus, demonstrating lack of apical polarity and high-lighting the spot-like adhesion points on lateral cell surfaces. Movie 1 (doi: 10.6084/m9.figshare.3141928) can be viewed at FigShare: https://figshare.com/articles/Jorgens_et_al_JCS_2016_Movie_1/3141928

Journal of Cell Science • Supplementary information

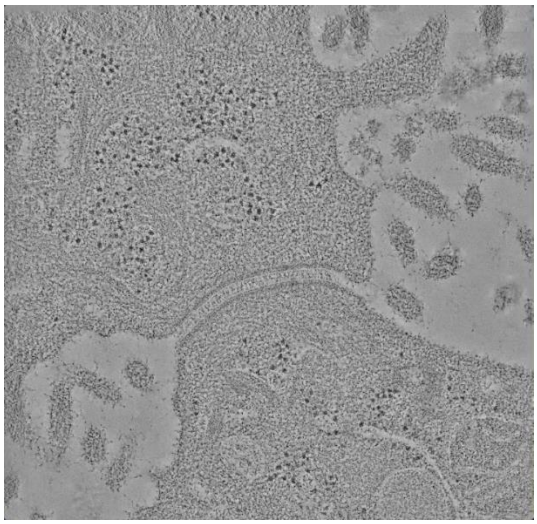

Movie 2: High resolution electron tomography of desmosome cell junction. Electron tomogram of a 100 nm thin section imaged every 1° from 70° to 70°. The nominal setting of defocus was 1 micrometer, and the pixel size of the data corresponded to 1 nm. The ultrastructural composition of the desmosome junction is visualized. Filaments between electron dense plaques on adjacent cell membranes are observed to span a gap of ~ 30 nm. Cytoskeletal filaments are observed linking into the electron dense plaques. Movie 2 (doi: 10.6084/m9.figshare.3167950) can be viewed at FigShare: https://figshare.com/articles/Jorgens_et_al_JCS_2016_Movie_2/3167950

Journal of Cell Science • Supplementary information

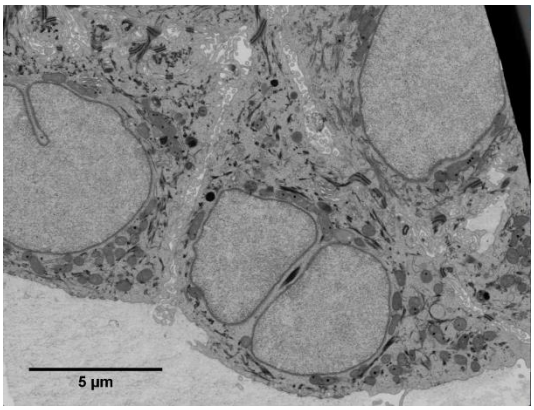

Movie 3: FIB-SEM of part of a S1 acinus with nuclear invaginations and tunnels. FIB-SEM was collected on the S1 acinus for a final voxel dimension of 4 nm^3. The left and right most cells each have deep nuclear invaginations (NR type II). A primary cilium is observed at the beginning of the dataset on the apical surface of the central cell. The central displays both nuclear invaginations and cytoskeletal filaments transversing the nucleus within a tunnel. Movie 3 (doi: 10.6084/m9.figshare.3145006) can be viewed at FigShare: https://figshare.com/articles/Jorgens_et_al_JCS_2016_Movie_3/3145006

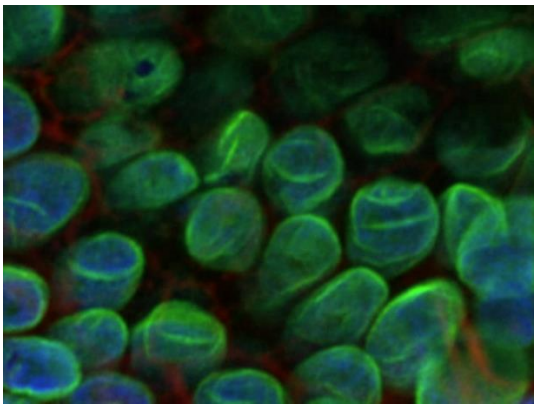

Movie 4: Lamin B1 stain of human mammary ductal cells. Confocal stack of a duct in a cryosection of human mammary tissue stained for DNA (DAPI, blue), lamin B1 (green), & F-actin (phalloidin, red). Movie 4 (doi: 10.6084/m9.figshare.3145030) can be viewed at FigShare: https://figshare.com/articles/Jorgens_et_al_JCS_2016_Movie_4/3145030

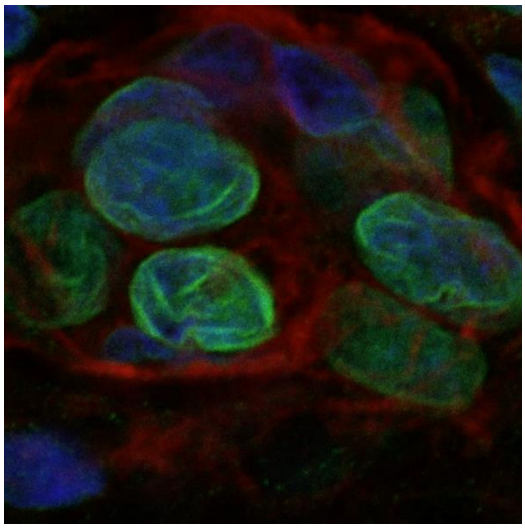

Movie 5: Lamin B1 stain of human mammary acinar cells. Confocal stack of an acinus in a cryosection of human mammary tissue stained for DNA (DAPI, blue), lamin B1 (green), & F-actin (phalloidin, red). Movie 5 (doi: 10.6084/m9.figshare.3145027) can be viewed at FigShare: https://figshare.com/articles/Jorgens_et_al_JCS_2016_Movie_5/3145027

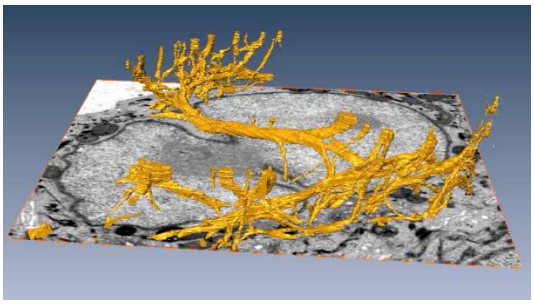

Movie 6: Segmented nuclear tunnel and cytoskeletal filament from FIB-SEM. The central cell nuclei from Movie 3 is segmented to reveal the 3D architecture of the cytoskeletal filament transversing the nucleus within a tunnel, rendered in yellow. Visualization of the 3D segmentation was performed with Amira software (FEI, Inc.). Movie 6 (doi: 10.6084/m9.figshare.3145063) can be viewed at FigShare: https://figshare.com/articles/Jorgens_et_al_JCS_2016_Movie_6/3145063

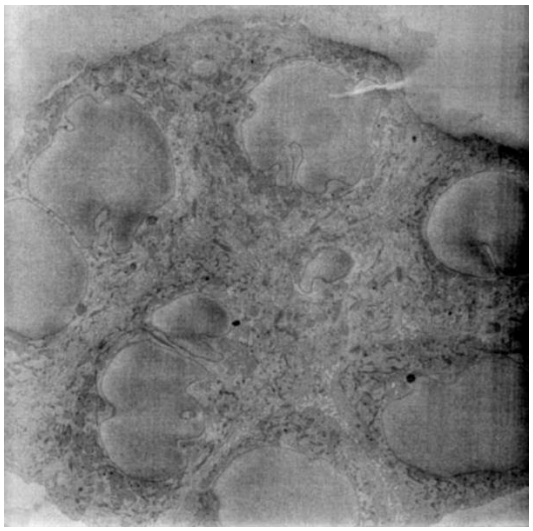

Movie 7: SBF-SEM of a S1 acinus with nuclear invaginations and tunnels. An acinus was imaged via SBF-SEM for a final voxel dimension of 50 nm^3. Cells are observed at various z-depths without and with deep nuclear invaginations (NR type II) and two cells display nuclear tunnels with cytoskeletal filaments. Movie 7 (doi: 10.6084/m9.figshare.3145012) can be viewed at FigShare:
https://figshare.com/articles/Jorgens_et_al_JCS_2016_Movie_7/3145012

Journal of Cell Science • Supplementary information

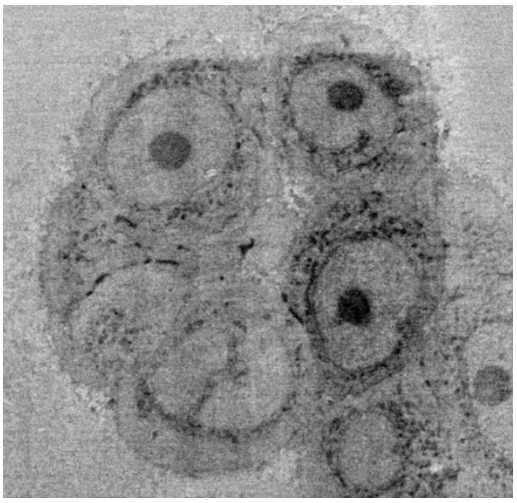

Movie 8: S1 acinus imaged by SBF-SEM. SBF-SEM data set collected of a S1 acinus, displaying eight whole and partially imaged cells. Five of the cells contain nuclear invaginations, three cells (37%) have nuclear tunnels with a total of four tunnels observed (two in one cell and one in each other cell). One cell has neither feature. Pixel size is ~100 nm^3. Movie 8 (doi: 10.6084/m9.figshare.3466046) can be viewed at FigShare: https://figshare.com/articles/Jorgens_et_al_JCS_2016_Movie_S1/3466046

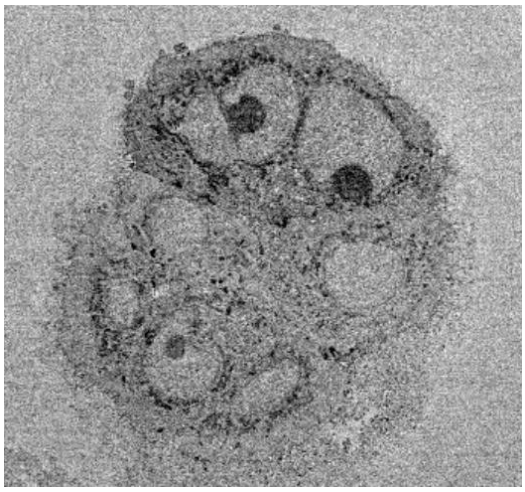

Movie 9: S1 acinus imaged by SBF-SEM. SBF-SEM data set collected of a S1 acinus, displaying six whole and partially imaged cells. Four of the cells contain nuclear invaginations, two cells (33%) have nuclear tunnels with a total of four tunnels observed (three in one cell and one in the other). Two cells do not display either feature. Pixel size is ~100 nm^3. Movie 9 (doi: 10.6084/m9.figshare.3466049) can be viewed at FigShare: https://figshare.com/articles/Jorgens_et_al_JCS_2016_Movie_S2/3466049

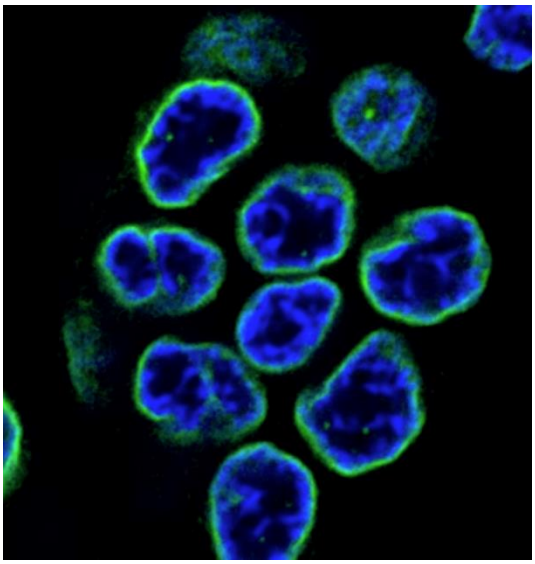

Movie 10: Lamin B1 stain of S1 acinus illuminates multiple nuclear tunnels and the NR. Confocal stack of staining for lamin B1 (green) and DNA (DAPI, blue) in growth arrested S1 acini. NR type II is observed in multiple cells as well as nuclear tunnels transversing the nucleus. Movie 10 (doi: 10.6084/m9.figshare.3145003) can be viewed at FigShare: https://figshare.com/articles/Jorgens_et_al_JCS_2015_Movie_8/3145003

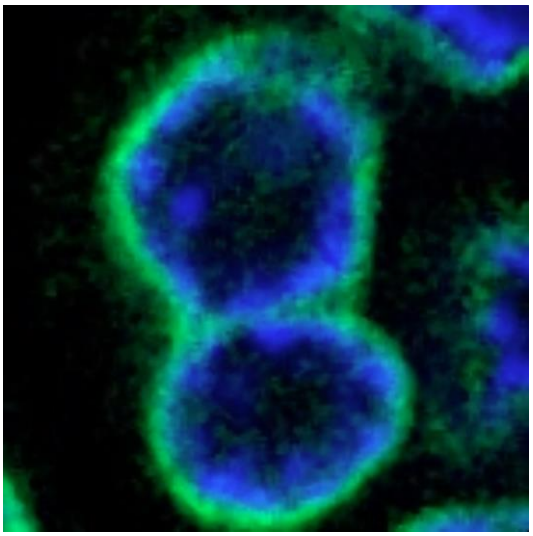

Movie 11: Lamin B1 stain of single cell illuminates a nuclear tunnel in a S1 acinus. Close up view of a single cell from the acinus in Movie 8 stained for lamin B1 (green) and DNA (DAPI, blue). A tunnel transversing the nucleus is observed. Movie 11 (doi: 10.6084/m9.figshare.3145021) can be viewed at FigShare: https://figshare.com/articles/Jorgens_et_al_JCS_2016_Movie_11/3145015

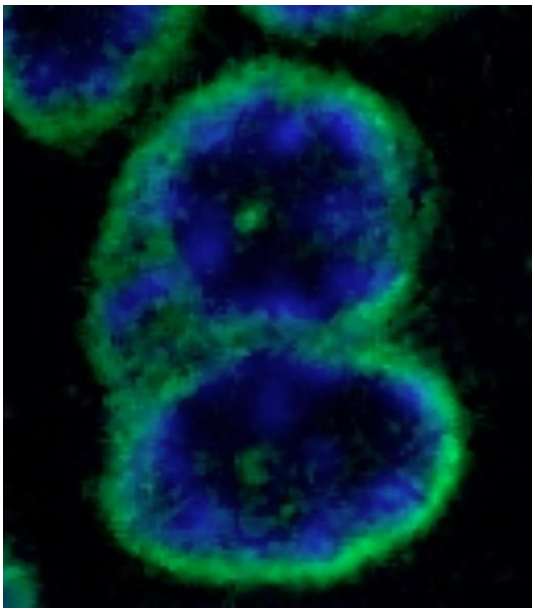

Movie 12: Lamin B1 stain of single cell illuminates a nuclear tunnel in a S1 acinus. Close up view of a second cell from the acinus in Movie 8 stained for lamin B1 (green) and DNA (DAPI, blue). A tunnel transversing the nucleus is observed. Movie 12 (doi: 10.6084/m9.figshare.3145018) can be viewed at FigShare: https://figshare.com/articles/Jorgens_et_al_JCS_2016_Movie_10/3145018

Journal of Cell Science • Supplementary information

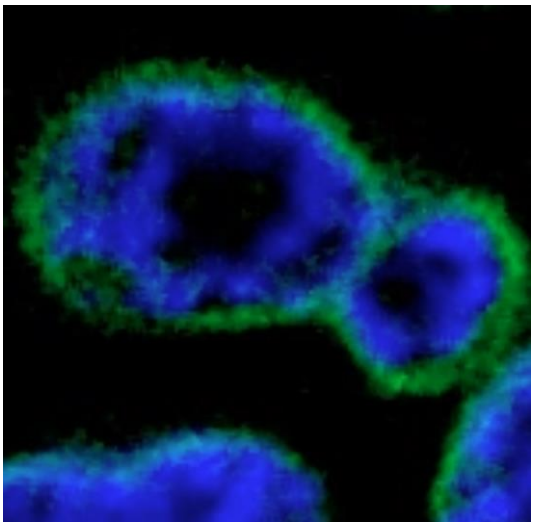

Movie 13: Lamin B1 stain of single cell illuminates a nuclear tunnel in a S1 acinus. Close up view of a third cell from the acinus in Movie 8 stained for lamin B1 (green) and DNA (DAPI, blue). A tunnel transversing the nucleus is observed. Movie 13 (doi: https://figshare.com/articles/Jorgens_et_al_JCS_2016_Movie_9/3145021

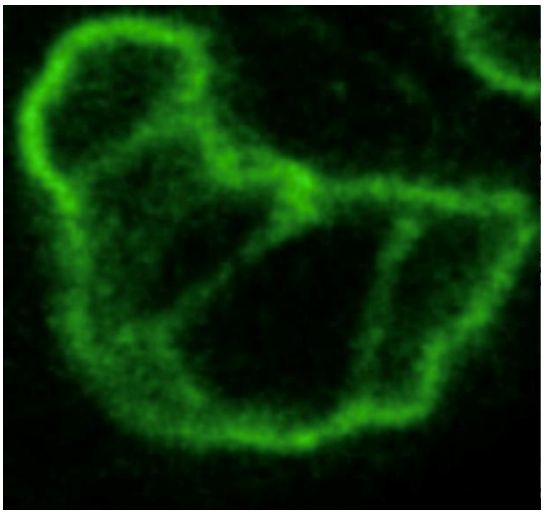

Movie 14: Lamin B1 stain illuminates four nuclear tunnels in a single S1 cell. Close up view of a single cell in an acinus stained for lamin B1 (green) and DNA (DAPI, blue) and imaged by confocal microscopy. Four tunnels traversing a single nucleus are observed. Movie 14 (doi: 10.6084/m9.figshare.3466052) can be viewed at FigShare: https://figshare.com/articles/Jorgens_et_al_JCS_2016_Movie_S3/3466052

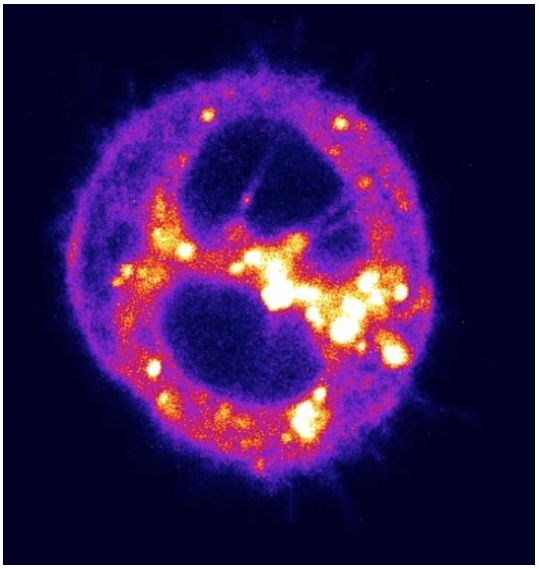

Movie 15: Live S1 cells stained with a membrane dye. Confocal stack of live S1 cells stained with the lipophilic membrane dye Vybrant DiI after 24 hours in 3D lrECM culture. The membrane dye stains the nuclear membrane illuminating multiple tunnels transversing the nucleus. Movie 15 (doi: 10.6084/m9.figshare.3145024) can be viewed at FigShare: https://figshare.com/articles/Jorgens_et_al_JCS_2016_Movie_12/3145024